222 (2023) 211454

Contents lists available at ScienceDirect

Geoenergy Science and Engineering

journal homepage: www.sciencedirect.com/journal/geoenergy-science-and-engineering

Evolution of the hydrocarbon migration system of the lower enping formation in the pearl river estuary basin

Shengmin Huang [a,b], Hong Pang [a,b,*], Kuiyou Ma [a,b], Hongbo Li [c], Lili Zhang [c], Sa Yu [c]

[a] China University of Petroleum (Beijing), Beijing, 102249, China
[b] State Key Laboratory of Petroleum Resources and Prospecting, Beijing, 102249, China
[c] CNOOC (China) Co. Ltd. Shenzhen Branch, Shenzhen, 518000, Guangdong, China

ARTICLE INFO

Keywords:
Oil and gas resources
Oil and gas accumulation model
Hydrocarbon expulsion threshold
Pearl river estuary basin
Lufeng sag

ABSTRACT

The Enping Formation of the Paleogene System in the Lufeng south area of the Pearl River Estuary Basin has good potential for hydrocarbon exploration. It is characterized by a vertically large distribution of a crude oil type and a widely horizontal distribution of similar crude oil. With the complex characteristics of hydrocarbon distribution and migration, studying the evolution mode of this migration system on a dynamic scale is necessary. In this study, the key accumulation period was determined using existing logging, seismic, and microscopic data combined with fluid inclusion and burial history. Then, the system's migration path and the direction of migration in the key accumulation period were analyzed, and the migration system and evolution model in the study area were established. The results show two stages of accumulation in the southern Lufeng area: 19–8 Ma and 8–0 Ma. In the first stage, the reservoir mainly followed the transport of a far-source fault–sand–ridge coupling system and the traps on the migration path were favorable for hydrocarbon accumulation. In the second accumulation period, traps that developed near the oil-source faults were favorable for hydrocarbon accumulation. The favorable traps in the first accumulation period were distributed in the whole area. The traps in the southwest wells B921 and C1211 were larger than the first stage, whereas the favorable traps in the northeast and central parts were mainly distributed in B211D and its adjacent well area, with smaller and scattered traps. Favorable traps in the second accumulation period were mainly distributed in the eastern and central regions, around wells B211D and B161, whereas the traps in the southwest were not conducive to hydrocarbon accumulation due to the lack of effective transport system connection. The results of this study have a certain guiding significance for practical exploration.

1. Introduction

Hydrocarbon migration is the synthesis of several physical processes involving long-duration geological processes (Zhang et al., 2010; Luo et al., 2012). In this regard, simulating transport processes is always a difficulty in petroleum geology research, as first started by Hubbert (1953). Fluid potential was used to indicate the direction of fluid migration in his research. Later, England et al. (1987) introduced the concept of oil potential based on fluid potential and reported that oil and gas always migrate along the direction of the smallest oil potential. They proposed various indicators of the direction of hydrocarbon migration (England et al., 1987). Before the 21st century, studies on the migration system focused on a single migration element. Chandler et al. (1989) and Dreyer et al. (1990) investigated core data and outcrops and found very close relationships between sand permeability and sedimentary facies. Smith (1980) studied the role of sealed and unsealed faults in hydrocarbon migration and found that the influence of faults on hydrocarbon migration in the later period mainly depends on the lithology of the joint between two plates of the fault. Hooper (1991) studied the role of growing faults during fluid migration and found that fluid migration in faults comprises multiple stages. Gibson (1994) studied the faults of siliceous clastic rock strata and found that mudstone smear is also important for fault sealing. Bethke et al. (1991) investigated unconformities as well as the formation of oil and gas reservoirs and found that unconformities act as channels for oil and gas migration.

From the 1990s to the beginning of the 21st century, researches on migration systems began to change from microscale to macroscale, qualitative to quantitative, and single-factor to multifactor coupling

---

* Corresponding author. China University of Petroleum (Beijing), Beijing, 102249, China.
E-mail address: panghong19820107@126.com (H. Pang).

https://doi.org/10.1016/j.geoen.2023.211454
Received 29 June 2022; Received in revised form 26 November 2022; Accepted 8 January 2023

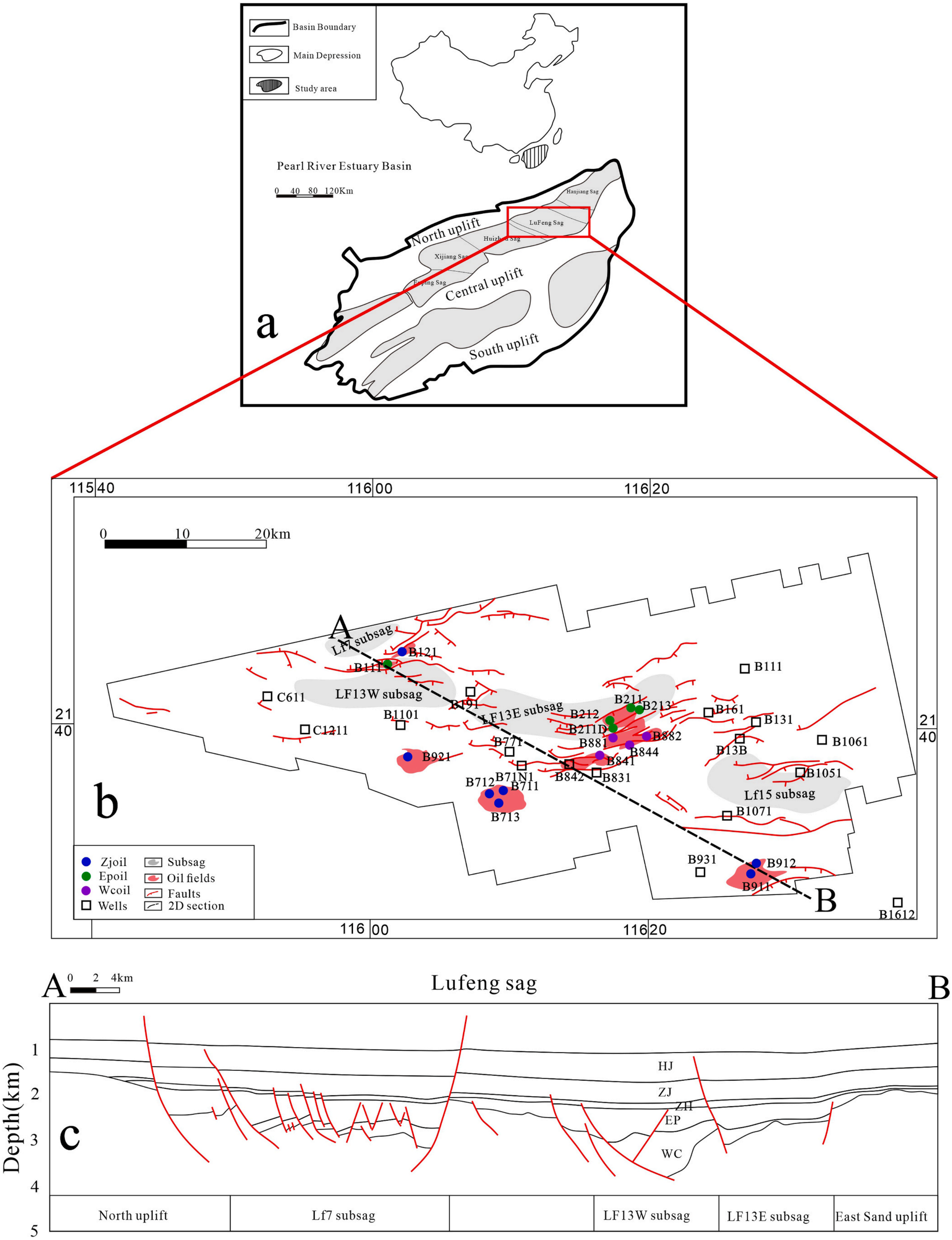

Fig. 1. Schematic diagram of the geological survey in the southern Lufeng area. (a) Schematic diagram of the geographical location of the Zhu I depression in Pearl River Mouth Basin. (b) Lufeng south structure scope and reservoir distribution map. (c) Cross section of the southern Lufeng area.

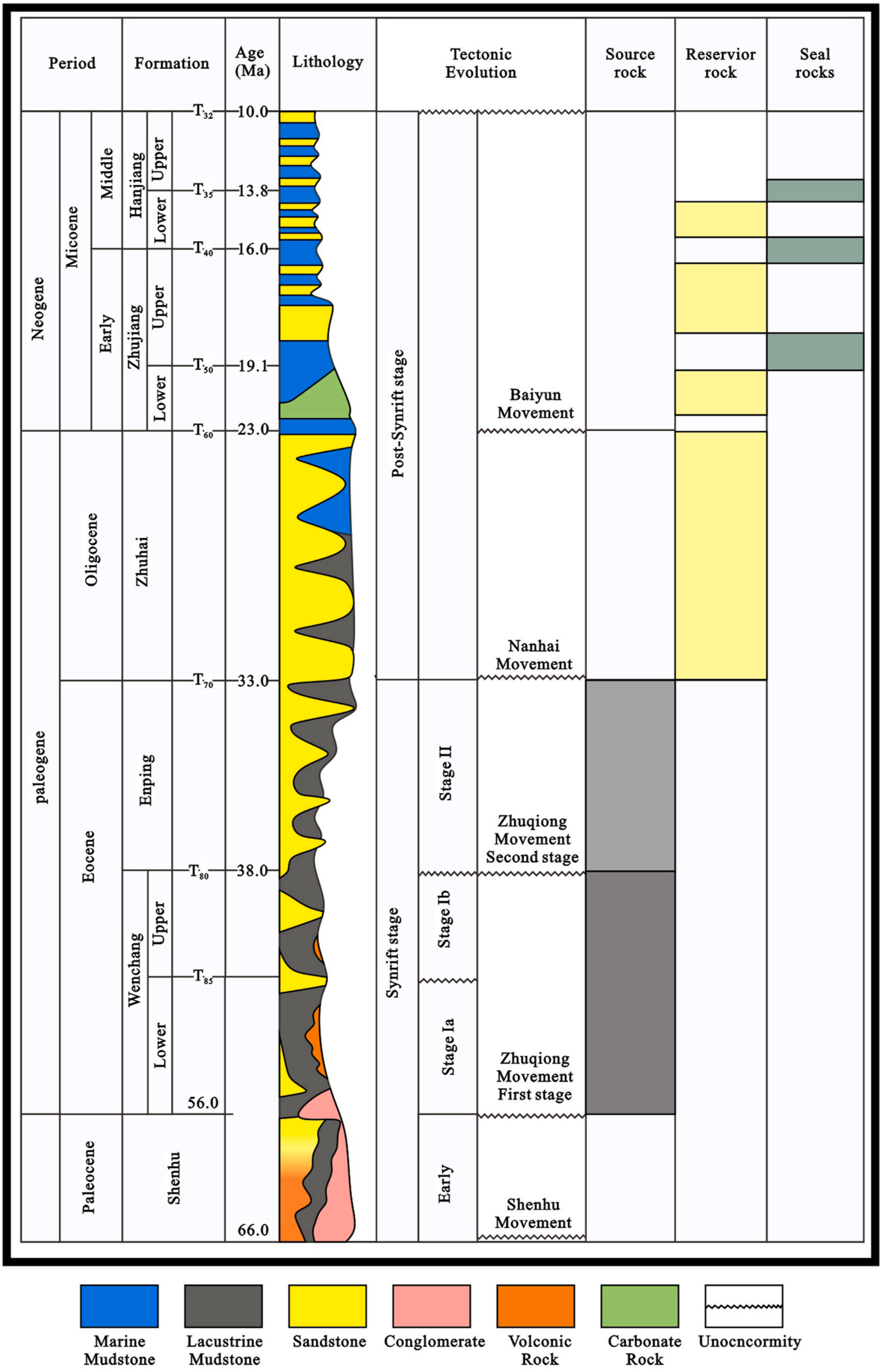

Fig. 2. Comprehensive stratigraphic histogram of the Zhu I depression.

conduction. Hunt (1990) analyzed the hydrodynamic system of most basins in the world and proposed the concept of fluid compartment, indicating multiple sets of different migration and accumulation units in the same basin. Galeazzi (1998) divided the petroleum migration system in their study area into a main transport system (composed of transport layers) and a secondary transport system (composed of fault transport layers) according to the characteristics of the basic elements of the petroleum system and the structural stratigraphic framework. D.Leythaeuser et al. (2000) summarized and prospected research methods on the secondary migration of oil and gas and indicated that dynamic and quantitative dynamic research is the key to paleofluid migration. The study of coupling systems thus became the main research topic.

Because of the rapid development of information technology from 2010 to present, basin modeling and numerical analysis related to migration system research have become mainstream. Based on this, the research on quantitative and migration and aggregation dynamics is further enriched. Luo et al. (2012) quantified transport layers according to the heterogeneity of the transport layers during secondary oil migration and proposed a sandstone connectivity probability model. After that, several coupled analysis studies on the migration systems of various basins emerged at home and abroad. Liu et al. (2017) considered the influence of mantle-derived gas charging on reservoirs in the simulation of the transport system of the Wen’an slope. Bourdet et al. (2019) used fluid inclusions to determine the hydrocarbon charging history of the Bight Basin and systematically restored the evolutionary history of the hydrocarbon migration path. Zhuravljov et al., 2021 explicitly and implicitly simulated migration trajectories and found that the implicit simulation was more consistent with reality because of its longer time span and more stable model. Wang et al. (2021) quantitatively analyzed oil and gas migration in the sandstone transporting layer of the Shahejie Formation in Bohai Bay Basin and recovered the migration system comprehensively. Luan et al. (2021) studied the influence of carbonate cementation controlled by faults on hydrocarbon transport in Dongying Sag and attributed the influencing factors of the transport system to fault activity. In addition, with the popularization of big data and artificial intelligence, many simulations of oil and gas migration used algorithms in recent years. For example, Wang et al. (2016) used the ant colony algorithm to numerically simulate hydrocarbon migration to find sweet spots in tight sandstones in the Ordos Basin.

At present, research on the migration system in the Lufeng area focused on the influence of sedimentary tectonics on the transport system and accumulation process. Peng et al. (2016) analyzed the hydrocarbon generation and expulsion of Eocene source rocks by establishing a hydrocarbon generation and expulsion model based on the pyrolysis data of source rocks in the Lufeng area. They specified the direction for the exploration of tight sandstone reservoirs. Wang et al. (2019) revealed the controlling effect of structures on reservoir formation by restoring the tectonic evolution of Lufeng 13 sag and combining it with petroleum geological evolution. Ge et al. (2021) focused on the analysis of the differences in sedimentary structural characteristics of different depressions to explore the main controlling factors of oil and gas enrichment and formulated the exploration idea of “optimizing the exploration of rich depressions and differentiating exploration.”

At present, three types of crude oils have been discovered in the southern Lufeng area, mainly showing large differences in vertical distribution and wide distribution of similar crude oils in the transverse direction. However, explaining the cause of the complex distribution of these three types of crude oils using the existing transport system is difficult. In addition, because of the multistage accumulation characteristics in the southern Lufeng area, revealing the distribution law of complex oil and gas using the existing static transport system is difficult. Therefore, studying the transport system in the southern Lufeng area on a dynamic scale is necessary to better clarify the mechanism of oil and gas distribution, migration, and accumulation in the Enping Formation in the southern Lufeng area and provide theoretical reference for oil and gas exploration in the research area.

2. Geological setting

The Pearl River Mouth Basin, the largest offshore oil-bearing basin in China, is distributed in the east of Hainan Island and the southwest of Taiwan. It is divided into a series of depressions from north to south by its northern, central, and southern uplifts (Ma et al., 2019). Zhu I depression is located between the northern and central uplifts (Fig. 1a). Lufeng depression is located in the middle and northern part of Zhu I depression, between the Hanjiang and Huizhou depressions. The section from northwest to southeast mainly includes the Lufeng 7, 13 east, 13 west, and 15 subdepressions. Lufeng south area mainly refers to the area south of the Lufeng 13 west subdepression (Fig. 1b and c).

The tectonic evolution of the southern Lufeng area is characterized first by faults and then by depressions (Lin et al., 2021; Zhang et al., 2017).

The Paleozoic tectonic evolution of the Lufeng Depression can be divided into the rifting stage, the fault-pass transition stage and the depression stage. In which the rifting stage is the main period of hydrocarbon-generating depression formation, the basin has been stretched several times, mainly forming NE-trending controlled depressional fractures, and the fault activity gradually ceased in the late rifting action. The period of fault and depression conversion is mainly the deposition period of Enping Formation, the second stage of Zhuqiong movement makes the whole Lufeng Depression exposed to uplift and denudation, the early stage is mainly fracture activity, the late stage is dominated by depression activity. During the depression stage the basin came into overall subsidence and formed regional overlying strata: the Zhujiang and the Zhuhai Formation. During the deposition of the Hanjiang Formation, it entered the late stage of fracture activity, and the activation of the early NWW-trending fractures occurred, which had an important impact on the hydrocarbon transport and accumulation in the whole area.

Corresponding to the tectonic evolution, The deep lacustrine ofWenchang and Enping formations were mainly developed in the early stage of the rift(Ge et al., 2020), The lacustrine mudstone of Wenchang Formation distributed in the center of the depression and serves as the source rock of the whole area(Dai et al., 2019), Due to the uplift of the lake basin, delta facies began to develop in the late rifting stage. The Enping Formation sand body developed at the edge of the depression began to act as the reservoir(Zhu et al., 2019). The basin expands further during the depression stage, The whole area began to develop several sets of delta sand bodies, At this time, the Hanjiang Formation and Zhujiang Formation in Neogene formed several sets of reservoir and cap assemblages longitudinally(Dai et al., 2019). At present, oil and gas discoveries have been made in upper Wenchang Formation, Enping Formation, Zhuhai Formation and Zhujiang Formation (Fig. 1b). This study focuses on the lower Enping Formation of paleogene.

Delta facies reservoirs are mainly developed in lower Enping Formation in southern Lufeng area, which are in contact with source rocks of lower Wenchang Formation (Fig. 2). The main reservoirs were drilled at B211, B212, B213 and B211D in the middle uplift of East 13 subdepression, in addition to B111 at the northern edge of West 13 subdepression.

3. Method and data

First, the main accumulation periods of the southern Lufeng area were determined using fluid inclusions combined with burial history data. Then, the paleofluid potential was recovered, and the migration directions of oil and gas in different accumulation periods were determined using the paleofluid potential and the current crude oil density. Thereafter, source faults, sand bodies, and structural ridges in each accumulation period were recovered, and fault–sand–structural ridge coupling migration systems and evolution models in each accumulation period were established. Finally, favorable hydrocarbon accumulation areas were predicted according to the above model, and the reliability of

Table 1
Statistical table of crude oil density.

Well	Depth (m)	Density under15 °C (g/cm^3)	Density under20 °C (g/cm^3)
B111	**2703**	**0.8326**	**0.8291**
B111	**2922**	**0.8321**	**0.8285**
B111	**2517**	**0.8435**	**0.8402**
B212	**3704.5**	**0.8241**	**0.8207**
B212	**3704.5**	**0.8333**	**0.8299**
B213	**3600.2**	**0.8305**	**0.8271**
B213	**3445.6**	**0.8485**	**0.8452**
B213	**3445.6**	**0.8515**	**0.8482**
B213	**3445.6**	**0.85**	**0.8467**
B211D	**3234.84**	**-**	**0.8299**
B211D	**3240**	**-**	**0.8314**
B361	**2992.1**	**-**	**0.8691**
B71N1	**2580.1**	**0.8669**	**0.8669**
B71N1	**2901**	**0.8664**	**0.8631**
B71N1	**3381**	**0.8661**	**0.8628**
B843	**4167.8**	**0.8684**	**0.8651**
B844	**2450**	**-**	**0.8575**
B844	**2720**	**-**	**0.8505**
B881	**3328**	**0.832**	**0.832**
B881	**3842**	**0.8289**	**0.8255**
B881	**4600**	**0.8303**	**0.8269**
B881	**3663.78**	**-**	**0.8335**
B881	**3720**	**-**	**0.8335**
B881	**3620**	**-**	**0.8324**

Table 2
Core sample porosity test results.

WELL	Depth/(m)	Measured porosity(%)
B881	**3685.5**	**15.6**
B881	**3693.75**	**3.5**
B881	**3699**	**19.1**
B881	**3717.5**	**16.7**
B881	**3729.75**	**16.5**
B881	**3747.3**	**12.1**
B881	**3756.6**	**13.3**
B881	**3860.75**	**9.3**
B361	**2922.4**	**27.3**
B361	**2924.8**	**25**
B361	**2992.15**	**22.5**
B361	**2994**	**17.7**
B361	**3006.85**	**18.1**
B361	**3028.75**	**15.6**
B361	**3048.4**	**10**
B361	**3085.2**	**10.2**
B361	**3092.5**	**12.1**
B361	**3232.15**	**17.9**
B361	**3453.95**	**16.6**

the prediction results was verified.

A Nikon 80 I dual-channel microscope was used for the fluorescence identification of organic inclusions, and a French IHR320 Core 3 instrument was used for the microbeam fluorescence spectrum test. The microthermometry instrument for the inclusions was a Linkam THMS 600G equipped with a Leica DMLP polarizing microscope. During the temperature measurement, the initial heating rate was 10 °C/min, and changes in the inclusions were observed for 1 min every time the temperature was increased by 20 °C. When the bubble of the inclusions became smaller and approached the state of homogenization, the heating rate was adjusted to 2 °C/min.

The depth data used for fluid potential recovery were obtained using 3D seismic measurements in the work area. The crude oil density data directly used the crude oil density measured by drilling samples from 13 wells, with a total of 33 samples. The "Standard Test Method for Density and Relative Density of Crude Oils by Digital Density Analyzer ASTM D 5002–2013" was used as the standard for testing(details of operation in appendix). The data of crude oil density in the Lufeng area are presented in Table 1.

The reservoir porosity was derived from logging interpretation and laboratory measurements. A total of 149 data points from 22 wells were interpreted by logging (Table A). A total of 19 samples was measured from two wells in the laboratory using a CMS-300 (no. Zcsy-kfsy-088) equipment. According to the standard GB/T 29,172–2012 "Core Analysis Method" and SY/T 6385–1999 "Method for Determination of Rock Porosity and Permeability under Overburden," (details of operation in appendix) the sample porosity and permeability were measured and the results are given in Table 2.

The source rocks used to determine the threshold depth of

Table 3
Test results of accumulation periods.

Well	Formation	Accumulation period(Beginning)/Ma	Accumulation period(Ending)/Ma	Testing method
B211	**EP**	**9.8**	**6.4**	**Fluid Inclusion**
B211	**EP**	**4.9**	**0**	**Fluid Inclusion**
B7110	**EP**	**17.2**	**14.3**	**Fluid Inclusion**
B7110	**EP**	**7.2**	**3.1**	**Fluid Inclusion**
B711	**EP**	**14**	**12.5**	**Fluid Inclusion**
B821	**EP**	**10.3**	**7.6**	**Fluid Inclusion**
B141	**EP**	**14.6**	**10.3**	**Fluid Inclusion**

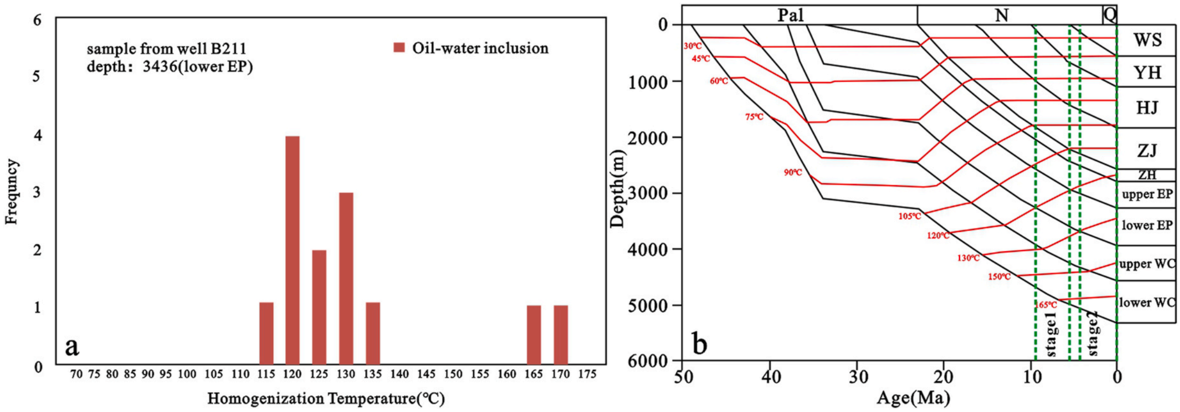

Fig. 3. Discriminant example of accumulation periods. (a) Histogram of the homogenization temperature in the Enping section of the B211 well. (b) Burial history map of well B211 (specific parameters in Table C).

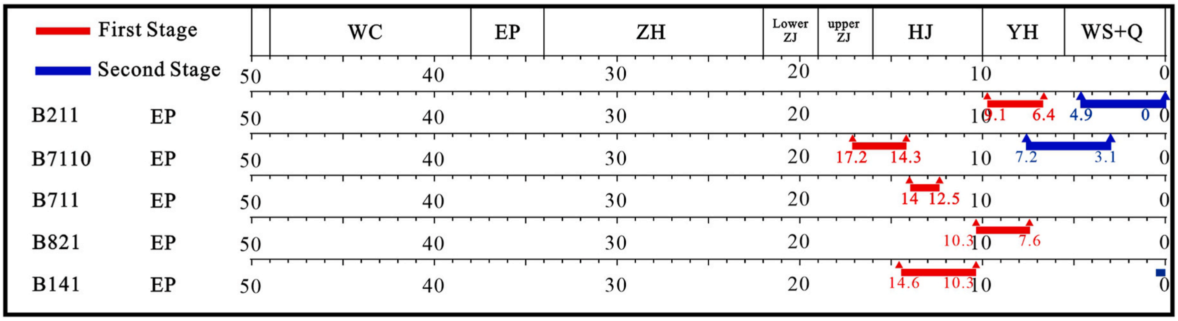

Fig. 4. Accumulation period of the Enping Formation in the southern Lufeng area.

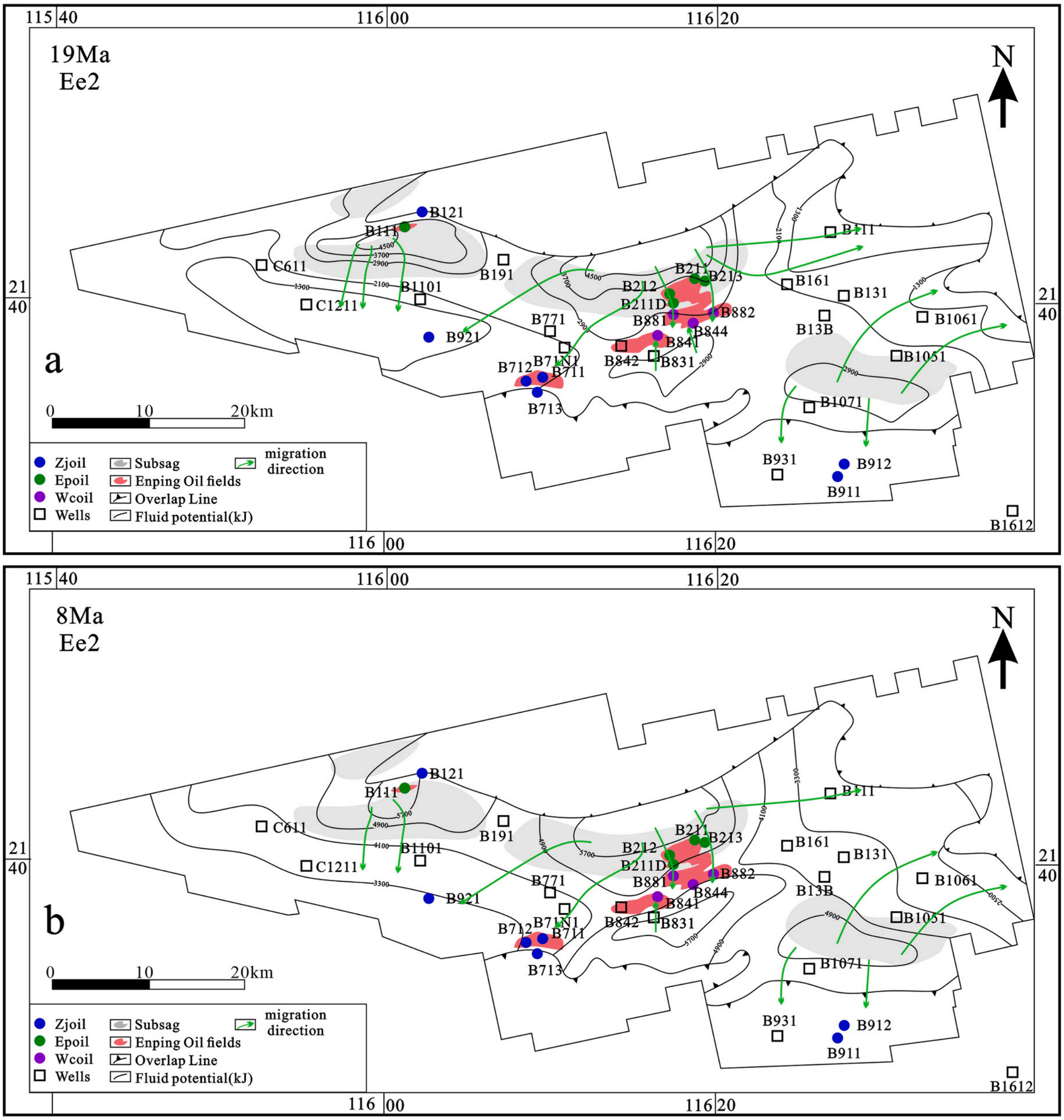

Fig. 5. Fluid potential distribution contour of the Enping Formation in the southern Lufeng area. (a) The first accumulation period. (b) The second accumulation period.

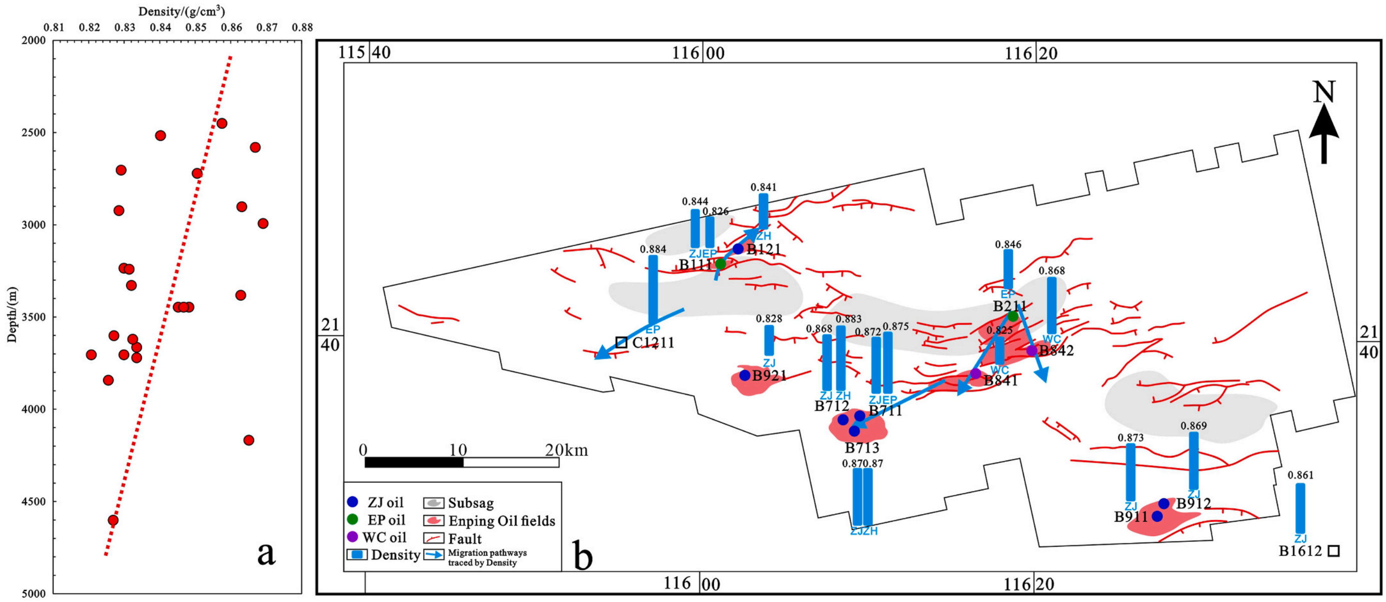

Fig. 6. Schematic diagram of the oil migration direction judging by the crude oil density in the southern Lufeng area. (a) Schematic diagram of the variation of crude oil density with depth. (b) Schematic diagram showing the migration direction of crude oil.

hydrocarbon generation came from 429 sample points from 24 wells in the whole area. The instrument used for this measurement was a Shimadzu GC-17A, Japan No. C10693201886SA, at a temperature of 27 °C and relative humidity of 55%. The measurement was conducted according to the implementation standard SY/T 5120–1997(details of operation in appendix) test data (Table B).

4. Results

4.1. Accumulation period

In this study, fluid inclusions were used to determine the accumulation period in the southern Lufeng area. Fluid inclusions are captured in diagenetic mineral crystal lattice defects or cracks. The homogenization temperature of fluid inclusions represents the lowest-temperature inclusions formed. The homogenization temperature of brine inclusions formed simultaneously as hydrocarbon inclusions represents the temperature at which oil and gas entered the reservoir. With improvements in inclusion detection technology, fluid inclusion research has been widely applied in determining hydrocarbon accumulation periods (Wang et al., 2020; Zhu et al., 2022). In this study, the fluid inclusions of 48 samples from different wells in different sections of the Lufeng southern area were microscopically observed. Then, the charging times of oil and gas were determined based on the thermal evolution history. Take well B211 as an example. The homogenization temperature histogram in Fig. 3 represents the core samples collected from the Enping Formation at a depth of 3436 m in well B211. The homogenization temperatures of the oil and water inclusions were 120 °C and 130 °C, respectively. The burial history map represents the burial history of the corresponding well B211. The homogenization temperatures of 120 °C and 130 °C in the lower Enping Formation correspond to 6.4–9.8 Ma and 0–4.8 Ma, respectively, in the burial history map (Fig. 3a and b).

The accumulation period data obtained using fluid inclusion analysis of the core samples of Enping Formation are shown in Table 3.

The above data are reflected in a statistical chart to obtain the distribution chart of the accumulation periods in the southern Lufeng area. The results show two periods of hydrocarbon charging in the Enping Formation in the southern Lufeng area: early stage (19–8 Ma) and late stage (8–0 Ma) (Fig. 4).

4.2. Direction of hydrocarbon migration

The Properties of oil and gas changes are usually observed during hydrocarbon migration (Zhang and Jin, 2000). Since Seifert and Moldowan (1978) used petroleum components to evaluate the migration distance, other predecessors have continuously explored this area and made significant progress (Horstad et al., 1995; Larter et al., 1996). In this study, the fluid potential was used in combination with the changes in crude oil density to determine the direction of oil and gas migration.

4.2.1. Fluid potential

The migration of free oil and gas in channels depends on the balance between the hydrodynamic force, capillary force, and buoyancy relative to the formation fluid (Hubbert, 1953; Berg, 1975; Schowalter, 1979; England et al., 1987). In this regard, England et al., 1987 introduced the concept of oil momentum in the process of secondary migration based on Hubbert (1953) to conveniently deal with the driving force of secondary migration of oil and gas (4.1).

$$\Phi_0 = v_0(\rho_w - \rho_o)gz \tag{4.1}$$

where Φ_0 is the oil potential, v_0 is the oil per unit volume, $\rho_w - \rho_o$ represents the density difference between the formation water and crude oil (g/cm^3), and g and z represent gravity acceleration (m/s^2) and burial depth (m), respectively. The oil potential field provides the direction and magnitude of the migration force and the oil and gas flow from high-to low-potential areas.

Crude oil density and buried depth are the key parameters of fluid potential analysis in the accumulation period. The crude oil density data were listed in Table 1. The burial depth was obtained using the layer flattening method (Yang et al., 2015) to recover the stratum structure in different accumulation periods. The main formation water density of 1.03 g/cm^3 and g of 9.8 m/s^2 were used to calculate the fluid potential in each accumulation period. Finally, the plane distribution of the fluid potential in different accumulation periods was obtained (Fig. 5).

Fig. 5 shows that the low-potential areas are mainly distributed in the northeast and southern edge of the southern Lufeng area. In addition, the transition zone between the eastern Lufeng 13 depression and the Lufeng 15 depression is also in the low-potential area. The distribution of high-potential areas is consistent with the distribution of subdepressions in the Lufeng sag. In the first accumulation period (19–8

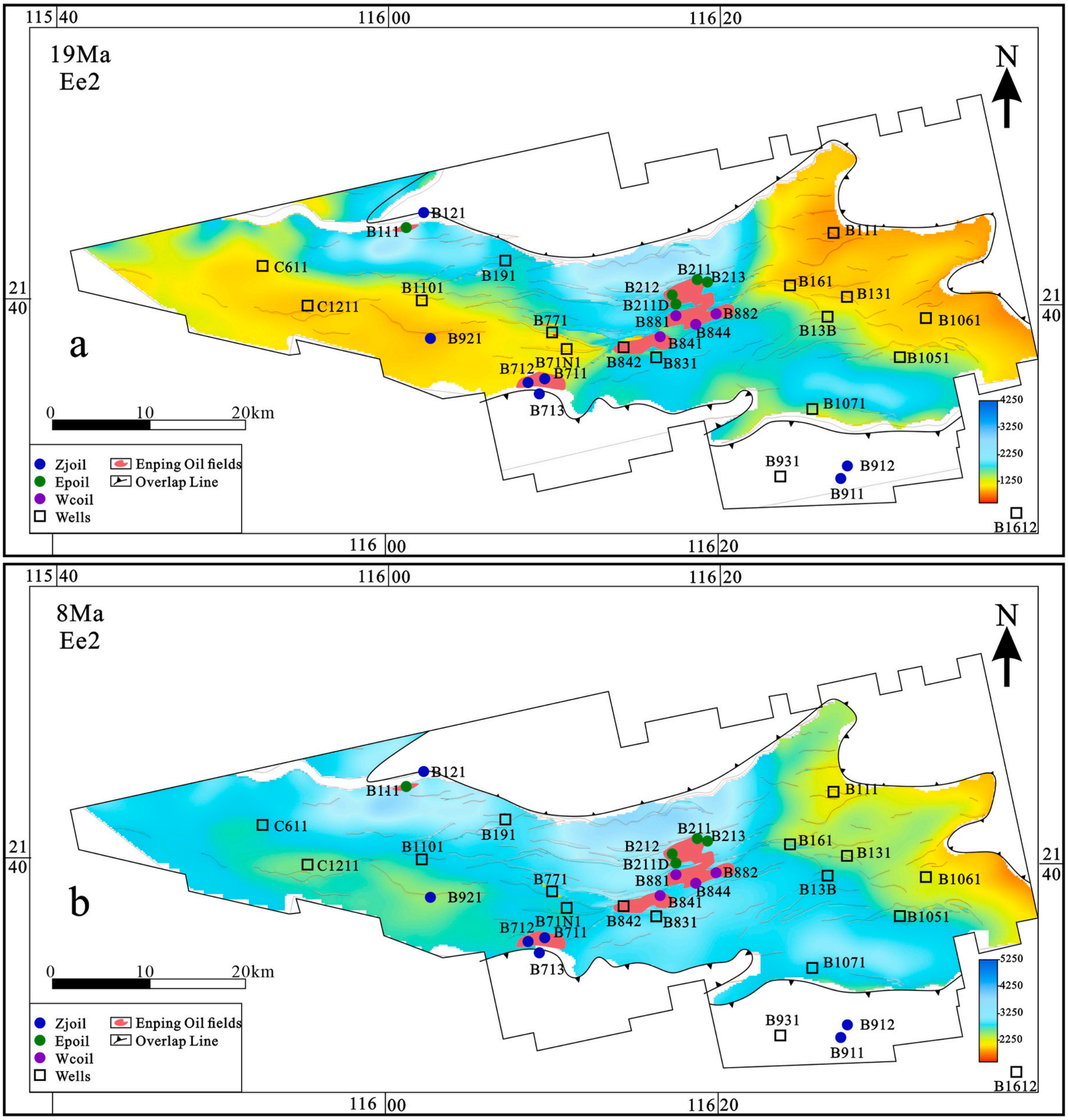

Fig. 7. Top surface structure diagram of the lower Enping Formation for the first (a) and second (b) accumulation periods.

Ma), the migration direction is mainly from B211, B212, and their adjacent wells to B882, B844, southwest to B712, B711, and northeast to B111. B111 goes south to B1101, B921, and other wells. The migration direction in the second accumulation period (8–0 Ma) is similar to that in the first one.

4.2.2. Crude oil density

Previous studies have shown that during hydrocarbon migration, the density of crude oil increases with increasing migration distance under the influence of oxidation (Trippetta et al., 2020; Ruggieri et al., 2022). In addition, in the case of multistage accumulation, the earlier the accumulation period, the greater the corresponding crude oil density. Chen et al. (2020) used the changes in the physical properties of oil, such as density and wax content, to indicate the direction of oil and gas migration in their study of Ordovician reservoirs in the Lunnan area of the Tarim Basin. They found that the closer the distance to the accumulation area, the higher the oil density.

The range of the density data of the Enping Formation in the southern Lufeng area is limited because of the few oil wells discovered in the area at present. Meanwhile, because the crude oil in the Lufeng area comes from the same set of source rocks of the Wenchang Formation, the physical properties of oil in the different formations can indicate the direction of oil and gas migration.

Given the variation characteristics of the crude oil density and burial depth, the crude oil density in the southern Lufeng area increased from 0.83 g/cm^3 below 4500 m to 0.86 g/cm^3 at 2500 m and tended to decrease with increasing burial depth (Fig. 6a).

Previous content have shown that the main reservoirs of the Enping Formation have two stages of accumulation, and the reason for the regular change in crude oil density may be caused by multistage accumulation, which is consistent with the reason for the change in crude oil density in the Lunnan area of the Tarim Basin. This reflects the characteristics of oil and gas migration from deep to shallow areas. From the characteristics of the oil density plane, the densities in wells B211 and B841 in the central depression are generally lower than those in B711 and its surrounding wells in the high part of the southern structure. This

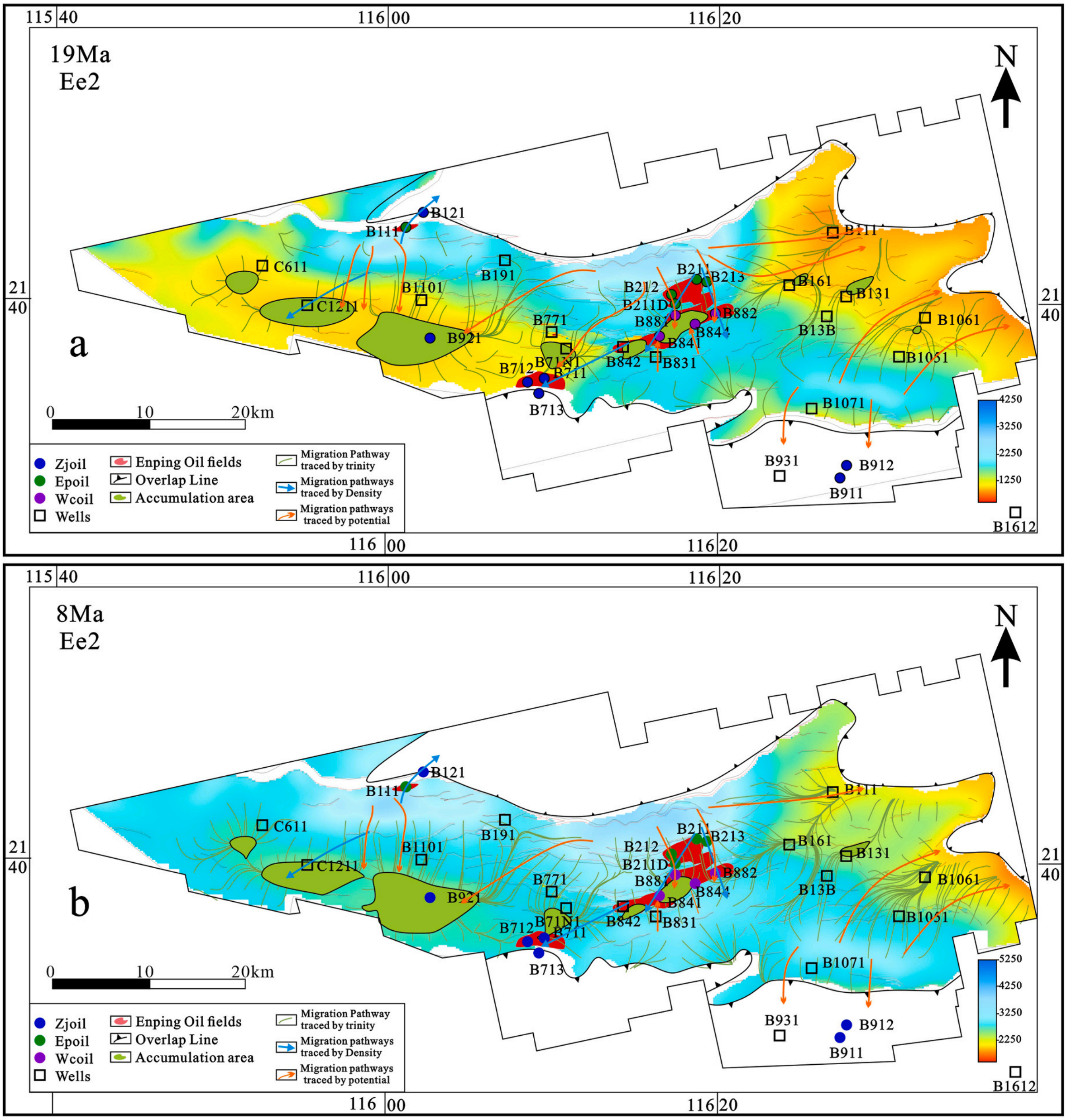

Fig. 8. Structural ridge distribution of the Enping Formation for the first (a) and second (b) accumulation periods.

indicates that the migration direction is from well B211 to B841, B842 to B711, and its adjacent wells. Similarly, the migration direction for the wells in the northwestern Lufeng southern area is from B111 to B121 (Fig. 6b).

4.3. Hydrocarbon migration pathway

4.3.1. Structure ridge

Inside the reservoir, hydrocarbons migrate upward to the top of the reservoir under the influence of buoyancy and then to the high part of the structure. Forming the line containing the highest point within the same rock layer, the structural ridge has a great convergence advantage (Xiang et al., 2004; Jiang et al., 2011). The distribution of tectonic ridges during the accumulation period affects the specific path of hydrocarbon migration (Li et al., 2019). Moreover, the specific form of tectonic ridges directly determines the upper limit of the hydrocarbon accumulation capacity of the aggregation unit.

Usually, the Trinity software is directly used to restore structural ridges. The basic principle is to construct an isogram based on a given base surface, determine the ridge line of the positive structure in the isogram, converge at the closed structural high point, and finally form the convergence area. The top surface structure of Enping in different accumulation periods should be first restored to obtain the distribution of structural ridges in different periods. In the second accumulation period, the current structure map is directly used. Thus, only the top surface structure of Enping in the first accumulation period must be restored.

The steps of structural ridge restoration mainly include using the layer flattening method to recover the top surface structure in the accumulation period and then importing the top surface structure data into the Trinity software to automatically simulate the structure ridge morphology. The main sedimentary strata from the first accumulation period to the present are the Hanjiang Formation and later strata. Therefore, the burial depth of the top structure of the lower Enping Formation in the present (the second accumulation period) should be subtracted from the top structure of the Hanjiang Formation to obtain

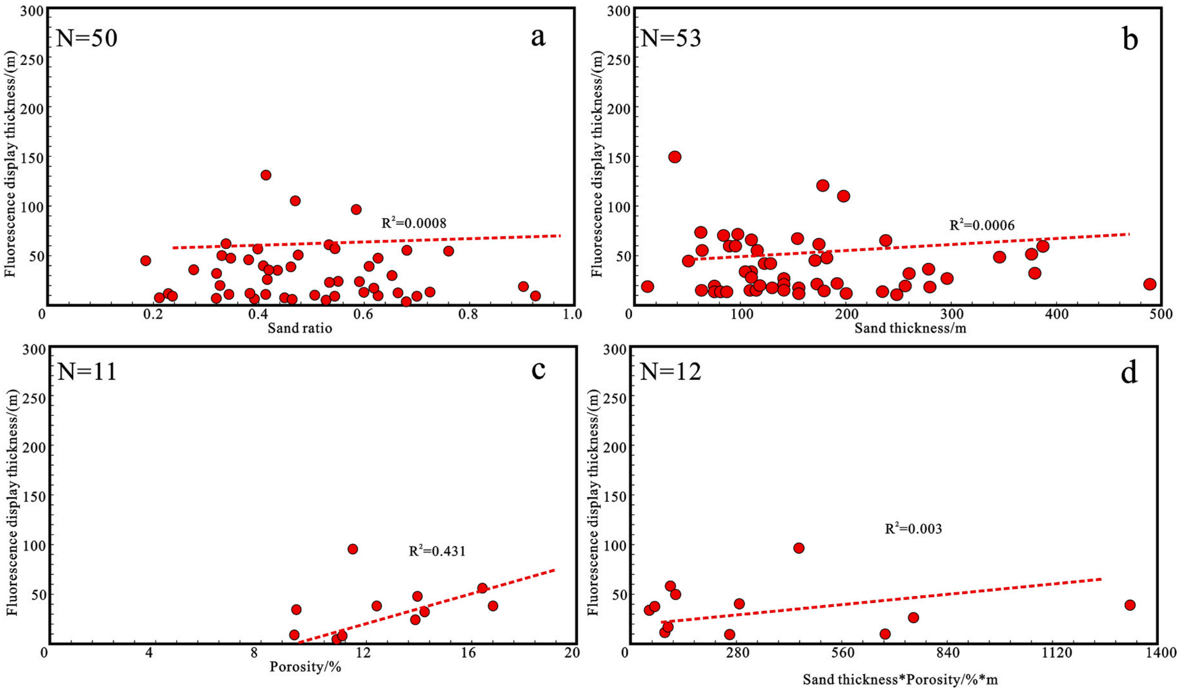

Fig. 9. Statistical representation diagram of conduction capacity. (a) Intersection diagram of the sand ratio and fluorescence thickness. (b) Intersection diagram of the sandstone thickness and fluorescence thickness. (c) Porosity–fluorescence thickness intersection diagram. (d) Intersection diagram of the pore thickness product and fluorescence thickness.

the lower Enping flat-top structure in the first accumulation period (Fig. 7a and b).

Fig. 7 shows that the burial depth of Enping in the first accumulation stage is ~1000 m lower than that in the second accumulation stage. In contrast, the tectonic amplitude in the early accumulation stage is larger than that in the late accumulation stage.

The structural maps obtained during each accumulation period were imported into the Trinity software to finally simulate the distribution of structural ridges in two periods (Fig. 8a and b). In the first accumulation period, the accumulation area of the structural ridges was mainly distributed southwest of the Lufeng sag, the transition zone between the eastern 13 sag and the eastern 15 sag, and part of the middle uplift area of the eastern 13 sag. The oil and gas that migrated northeast of the southern Lufeng area did not form an effective accumulation area. Compared with that in the first accumulation period, the accumulation range in the second accumulation period was relatively reduced. Still, the general distribution did not change much compared with that in the first accumulation period.

4.3.2. Sandstone transport system

Luo et al. (2012) defined sandstone transport conductors as geological bodies with pore space and permeability in the microscale, geometric connections of the sand body in the macroscale, and fluid dynamic connectivity in each part of the reservoir forming system within a certain spatiotemporal range. Sandstone transport conductors, as sand bodies with good continuity, good permeability, and strong connectivity in basins, constitute a large-scale and long-distance migration channel for oil and gas (Luo et al., 2020). The conductivity of sand bodies is affected by lithology, structure, porosity, permeability, and other aspects. Such conductors usually show strong heterogeneity (Yahi et al., 2001; Luo et al., 2013; Karlsen and Skeie, 2006). Therefore, finding the channel with the strongest conduction capacity in the region is necessary.

Hydrocarbon migration from the source rock is always along the path of minimum capillary force, and hydrocarbon residues bound in the pores of the transport layer traversed by the hydrocarbon usually show certain fluorescence characteristics. Therefore, the fluorescence thickness of the core can be used to represent the relative amount of oil and gas that passed through a certain conduction zone in geological history. The relative amount of hydrocarbon is used to directly characterize the conductivity of a sand body to hydrocarbons. In this study, the fluorescence thicknesses of the same sections in each well position were first used to judge the relative quality of the permeability of the reservoir to oil and gas. Then, reservoir indexes with better correlations with the fluorescence thicknesses were found. The obtained indexes were used to indirectly characterize the permeability of the reservoir.

In Fig. 9, the fluorescence thickness of the sand body at each well and the sand ratio of the reservoir, the thickness of the sand layer, and the product of porosity and thickness were respectively calculated. Four intersection plots were then obtained. By comparing the size of the four scatter plots R^2, the correlation between fluorescence thickness and reservoir porosity was relatively obvious. The fluorescence thickness is positively correlated with reservoir porosity, and the lower limit of the reservoir physical property corresponding to the minimum fluorescence thickness of 10% porosity. Based on the statistical results, reservoir porosity was used to characterize the transport capacity of the sand body in the Lufeng area, and the lower limit of porosity of the transporting sand body was set to 10%.

After obtaining the sand body's lower limit of permeability controlled by porosity, restoring the porosity plan of the sand body corresponding to the accumulation period is necessary to restore the permeability of the sand body in each reservoir formation period. During diagenesis, clastic rocks may undergo sedimentary diagenesis, such as compaction and cementation. After diagenesis, clastic rocks may undergo compression, dissolution, pressure solution, and other diagenetic epigeneses under the action of the formation fluid, pressure, and temperature. Compaction and cementation reduce the primary porosity and lead to porosity reduction(Zhang et al., 2022; Pan and Liu, 2022; Zhu et al., 2019; Ge et al., 2015). In contrast, dissolution and extrusion produce additional dissolution pores and fractures, resulting in increased porosity. Therefore, studying the pore composition of the reservoir in the southern Lufeng area is necessary to restore its

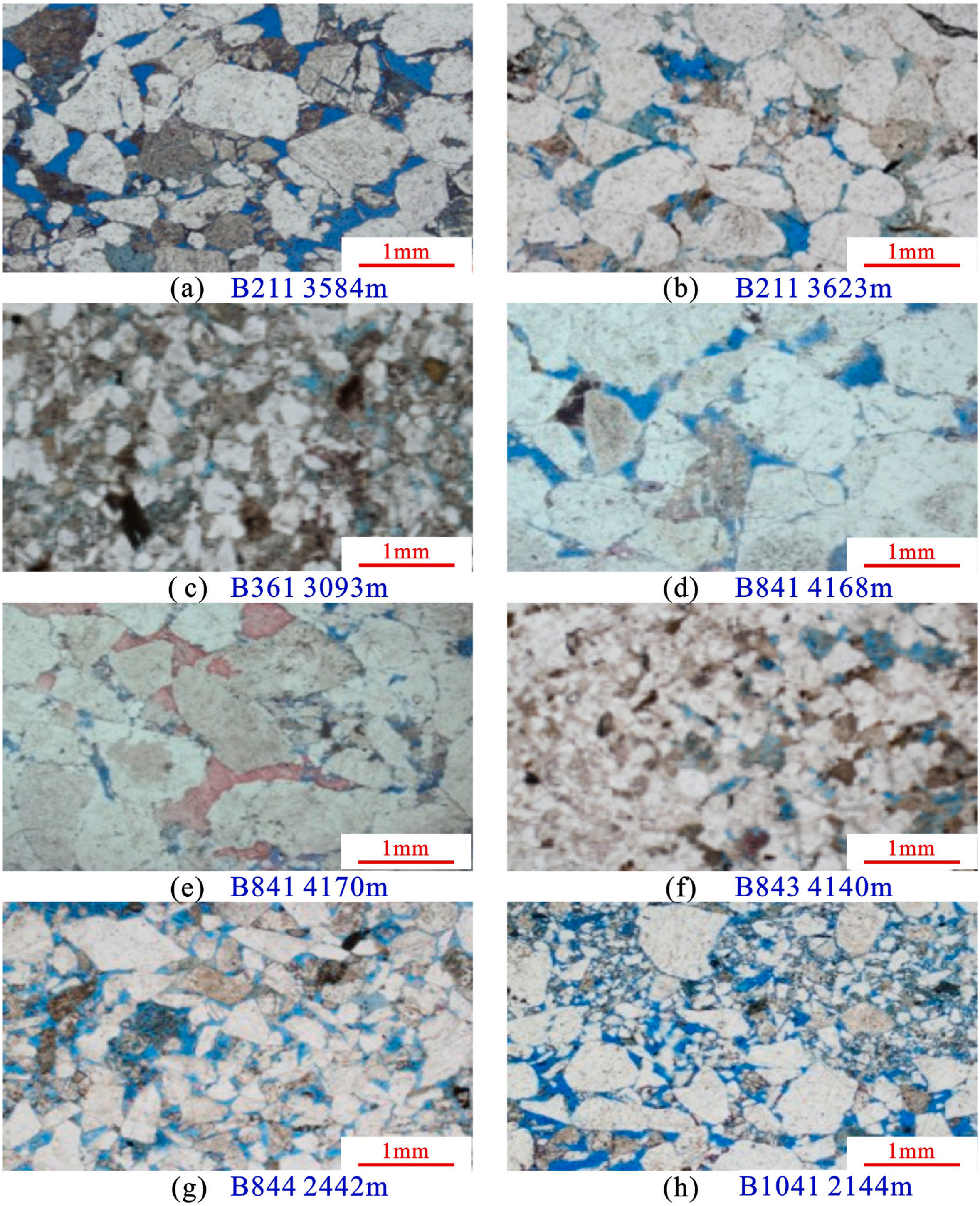

Fig. 10. Schematic diagram of reservoir pore space under microscope.

paleoporosity.

Eight samples from wells B211, B361, B841, B843, B844, and B1041 at different depths were observed using an optical microscope (Fig. 10). The figure shows that primary intergranular pores are the main pore types in the southern Lufeng area, whereas dissolution pores and fractures are rare. By comparing the microscopic images of the different depths in the southern Lufeng area, it is found that the main contact mode of the particles in the shallow layer (2000–3000 m) is tangential contact. In contrast, some particles in the middle and shallow layers (3000–4000 m) begin to show long contact, and the main contact mode of the clastic particles below 4000 m is mainly long contact. Therefore, the main pore reduction mechanism in the southern Lufeng area is compaction, and porosity is related to depth. Similarly, the good correlation between porosity and permeability also indicates that the lower Enping Formation reservoirs comprise mainly primary pores (Fig. 11).

The relationship between logging (AC, DEN, CNL) porosity and depth is obtained using the statistics of 160 porosity sample points from 21 wells in the southern Lufeng area. It is found that the porosity decreases linearly as the depth increases, and the specific equation is as follows:

$$P_0 = -H_0/106.2 + 46.8 \tag{4.2}$$

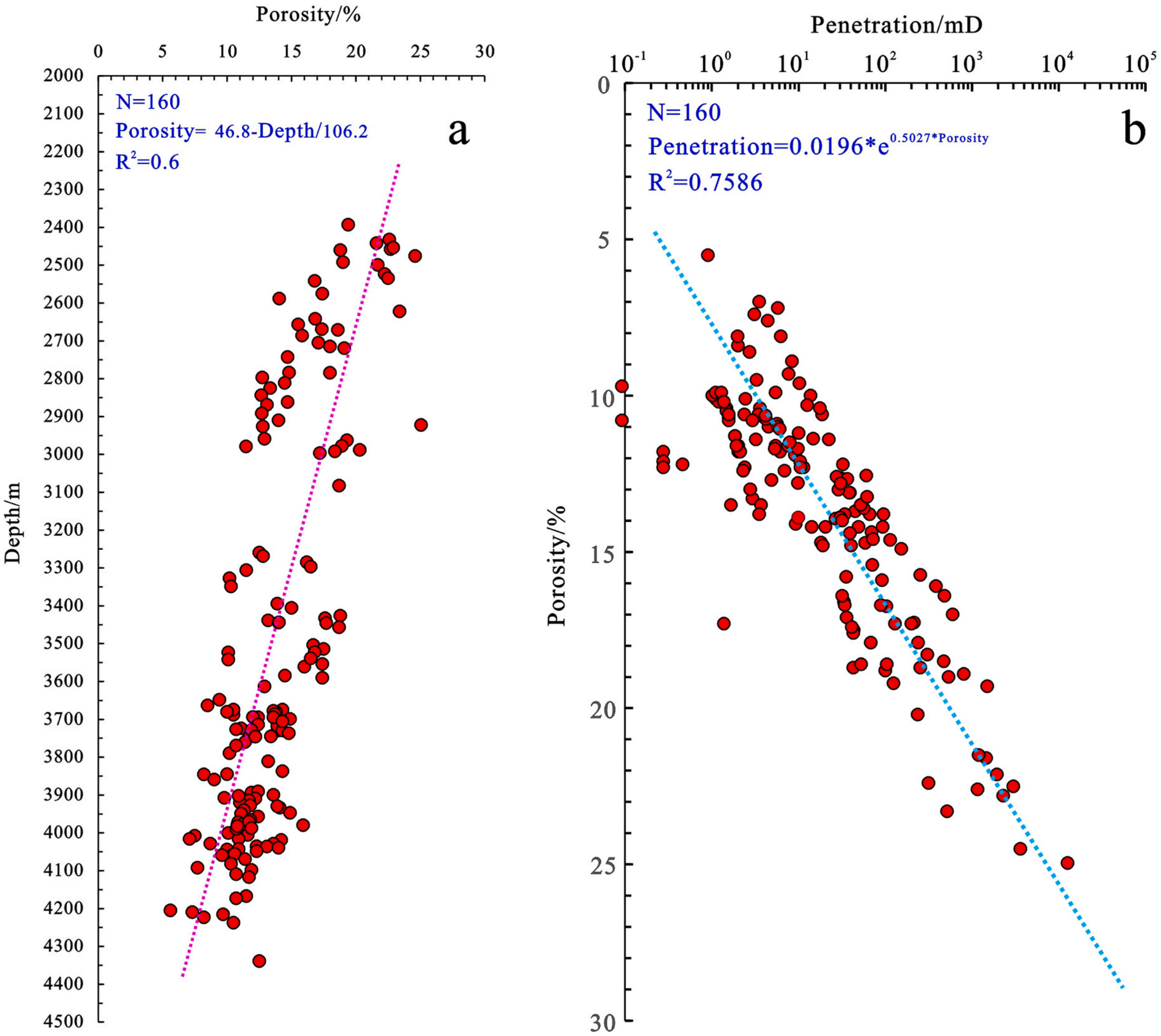

Fig. 11. Physical evolution of the reservoir. (a) Porosity–depth intersection diagram. (b) Porosity–permeability intersection diagram.

where P_0 represents the reservoir porosity and H_0 represents the reservoir burial depth. According to Equation (4.2), the porosity decreases by 9.42% at every 1000 m of deepening.

The structure diagram of the top surface of the two periods mentioned earlier was used as the buried depth of the reservoir during reservoir formation. Then, the plane distribution of the porosity of each well position was obtained using Equation (4.2) (Fig. 12a and b). The second accumulation period is the porosity distribution interpreted by logging at present, and the first is the porosity plane distribution recovered by combining the reduction value of porosity per unit burial depth with the current porosity. The figure shows that the recovered porosity value in the early stage is generally higher than that in the present because the burial depth is generally less than that today. The high-porosity area of the lower Enping Formation is mainly distributed in the east and west slope areas of the southern Lufeng area, where the delta channel sand body is usually developed. Areas of low porosity are generally distributed in the center of the depression, with areas of development of extensive lacustrine mudstones In addition, 10% porosity is taken as the lower limit of the effective sand body that can undertake the transport function. The whole area was dominated by the transporting sand body in the accumulation period. However, the transport capacities of the middle sand body (between B711 and B842) and the south sand body (between B1051 and B1071) are weak.

4.3.3. *Source fault*

Source faults play an important role in the process of hydrocarbon accumulation as vertical transport channels (Knipe, 1992; Ruggieri et al., 2022; Bense et al., 2003; Sibson et al., 1975). Previous studies have shown that the main structure of the fault is the fault core and the surrounding fracture zone. The fault core is a narrow zone consisting of the main sliding surface and the fault rock; the fracture zone is located at the perimeter of the fault core and consists mainly of fracture development zones and small faults.(Sibson et al., 1975; Narr, 1991; Billi et al., 2003). Under the action of tectonic stress, overpressure, or both, periodic episodic activity occurs (Hooper, 1991; Hao et al., 2004). There are differences in the transport capacity at different stages. On fluid migration in active fracture phases, Sibson et al., 1975 after studying the relationship between hydrothermal metalliferous ores and ancient fracture zones, noted that, Seismic fault activity acts like a pump, The thermal fluid is pumped from the deeper part and driven along the section into the upper tension fracture where the stress is lower, and the process is called seismic pumping. It is also noted that seismic pumps contribute to the transport of hydrocarbons in tectonically active areas. In the transport of hydrocarbons, the flow of fluids along growth fractures is considered to be cyclical and abrupt, and active fractures communicating with mature hydrocarbon source rocks can act as conduits for hydrocarbon migration (Hooper, 1991); When the fault is in a static state or a transitional period, it mainly follows the slow seepage mechanism controlled by buoyancy (Hooper, 1991; Pang et al., 2003).

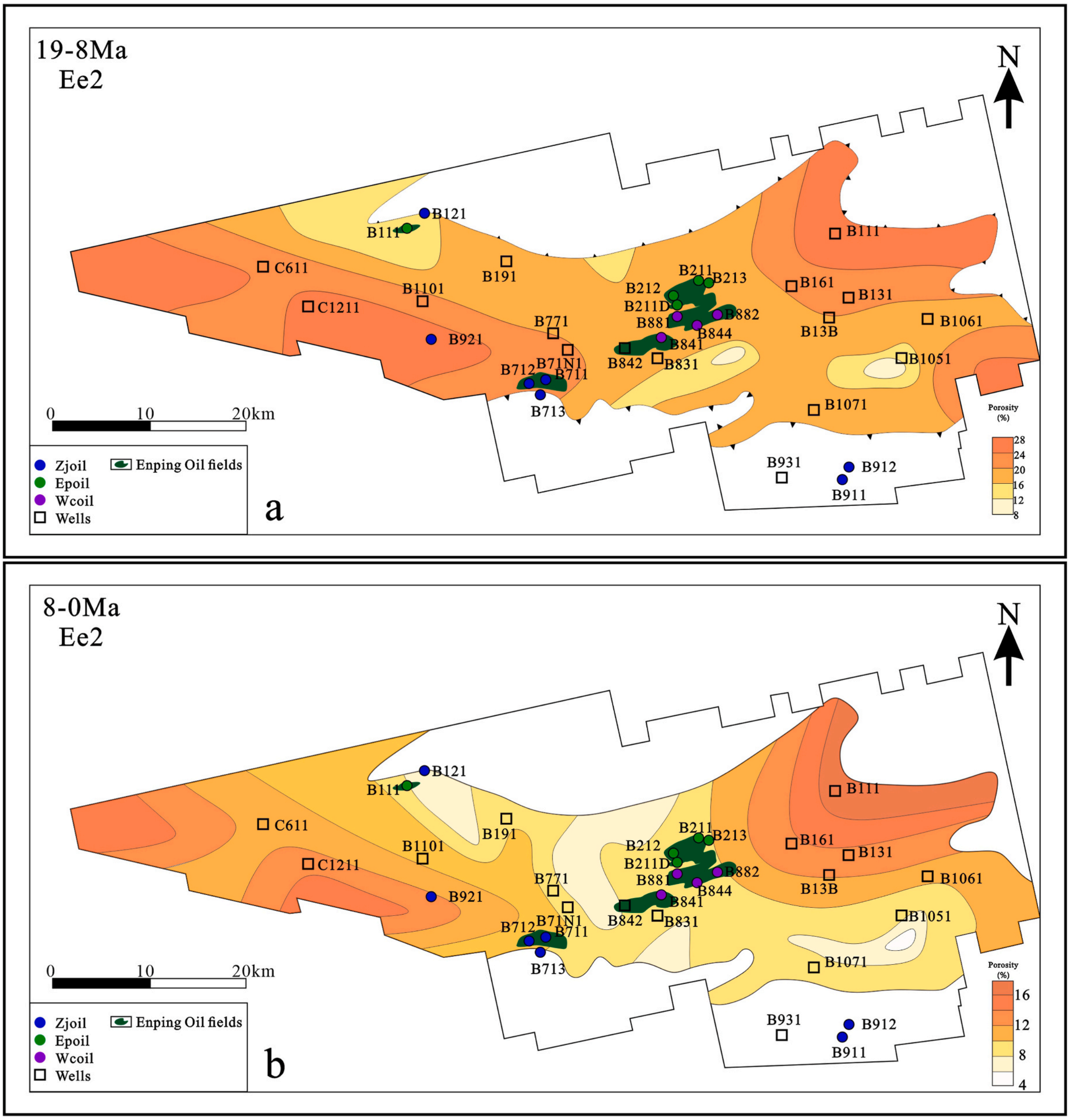

Fig. 12. Plane distribution of porosity in the lower Enping Formation in the southern Lufeng area for the first (a) and second (b) accumulation periods.

In this study, oil source faults are considered to be fractures that cut through discharged hydrocarbon source rocks, or other oil source faults (a sort of 2nd order source faults). In an example method, the expulsion degree is first calculated using the hydrocarbon generation potential evolution method (Chen et al., 2022) to determine whether the faults communicate with sources.

For the southern Lufeng area, the Wenchang Formation acts as a source rock (Ge et al., 2021; Dai et al., 2019). The depth corresponding to the effective source rock was determined by calculating the hydrocarbon generation potential index of the source rock using the data given in Table B (Fig. 13b). The final hydrocarbon expulsion threshold corresponds to a burial depth of 3500 m. Under the conditions of the first stage of accumulation, the burial depth of 3500 m corresponds to the mudstone of the lower Wenchang Formation in the whole area, i.e., only the mudstone of the Wenchang Formation in the first stage of accumulation can be used as a source fault (Fig. 13a,d). According to the discriminant results of the recovered profile in the first accumulation period, the faults on the plane are discriminated and the distribution of source faults is obtained. The distribution of source faults in the second accumulation period was obtained by following the same steps as those of the first accumulation period (Fig. 14).

In the first period (19–8 Ma), few source faults were observed, mainly distributed in the margin of the east LF13 depression. In the second accumulation period (8–0 Ma), with the expansion of the hydrocarbon expulsion range, source faults gradually extended to the center of the depression. The source faults mainly changed into some deep faults, and some shallow faults became source faults because of contact with previous source faults.

4.3.4. Migration system and evolution

After the migration direction, tectonic ridges, sand bodies, and source faults in each accumulation period were obtained, these four elements were superimposed to obtain the migration systems for each accumulation period. The evolution of the systems was summarized by comparing the differences between the systems of the two periods. As shown in Fig. 15, previous oil-source correlation results (Niu et al.,

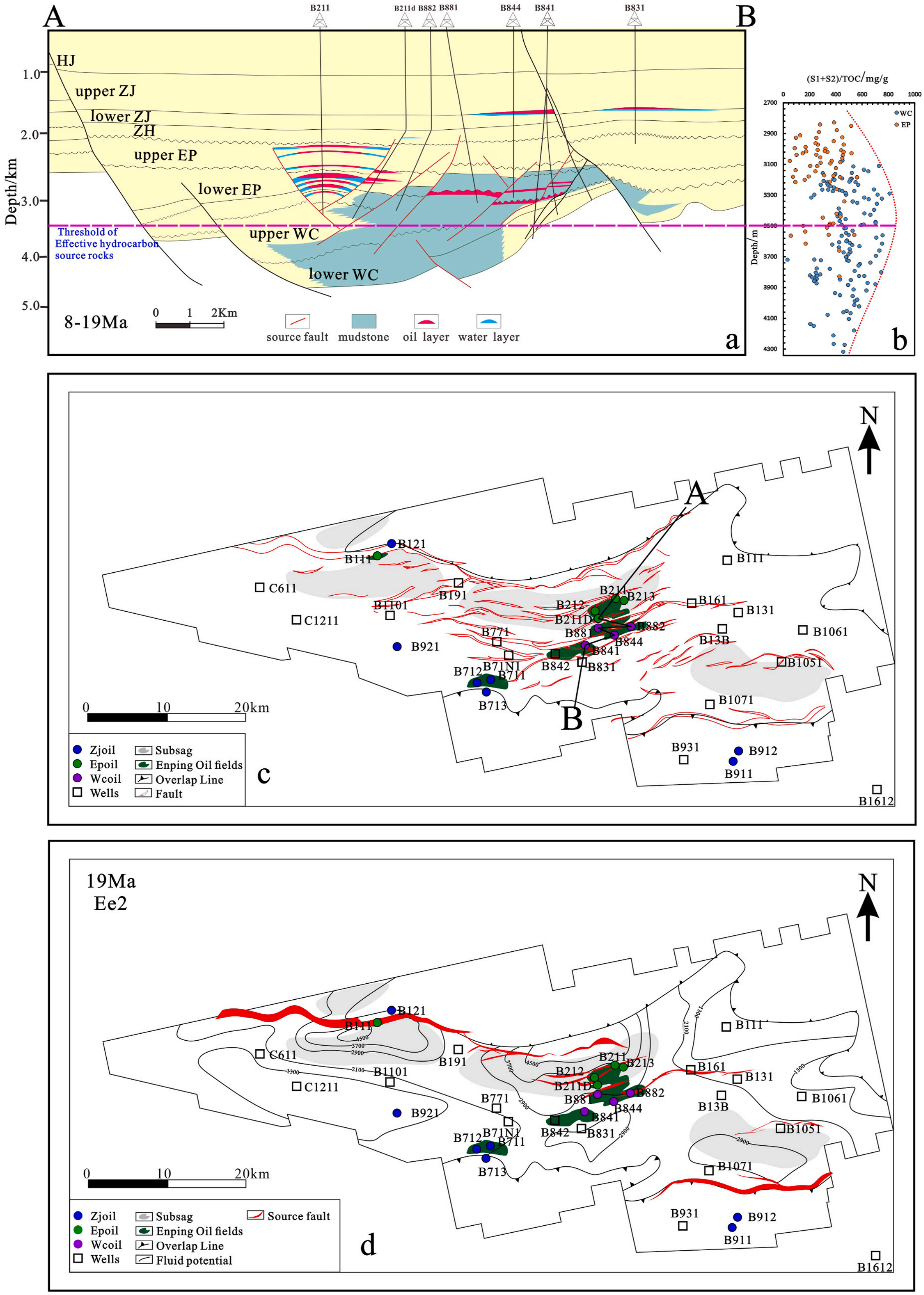

Fig. 13. Discrimination diagram of the source faults in the first accumulation period in the southern Lufeng area. (a) Schematic diagram of the source fracture profile. (b) Statistical chart of the depth corresponding to the hydrocarbon expulsion threshold. (c) Plane distribution of faults in the southern Lufeng area. (d) Plane distribution of source faults in the first accumulation period in the southern Lufeng area.

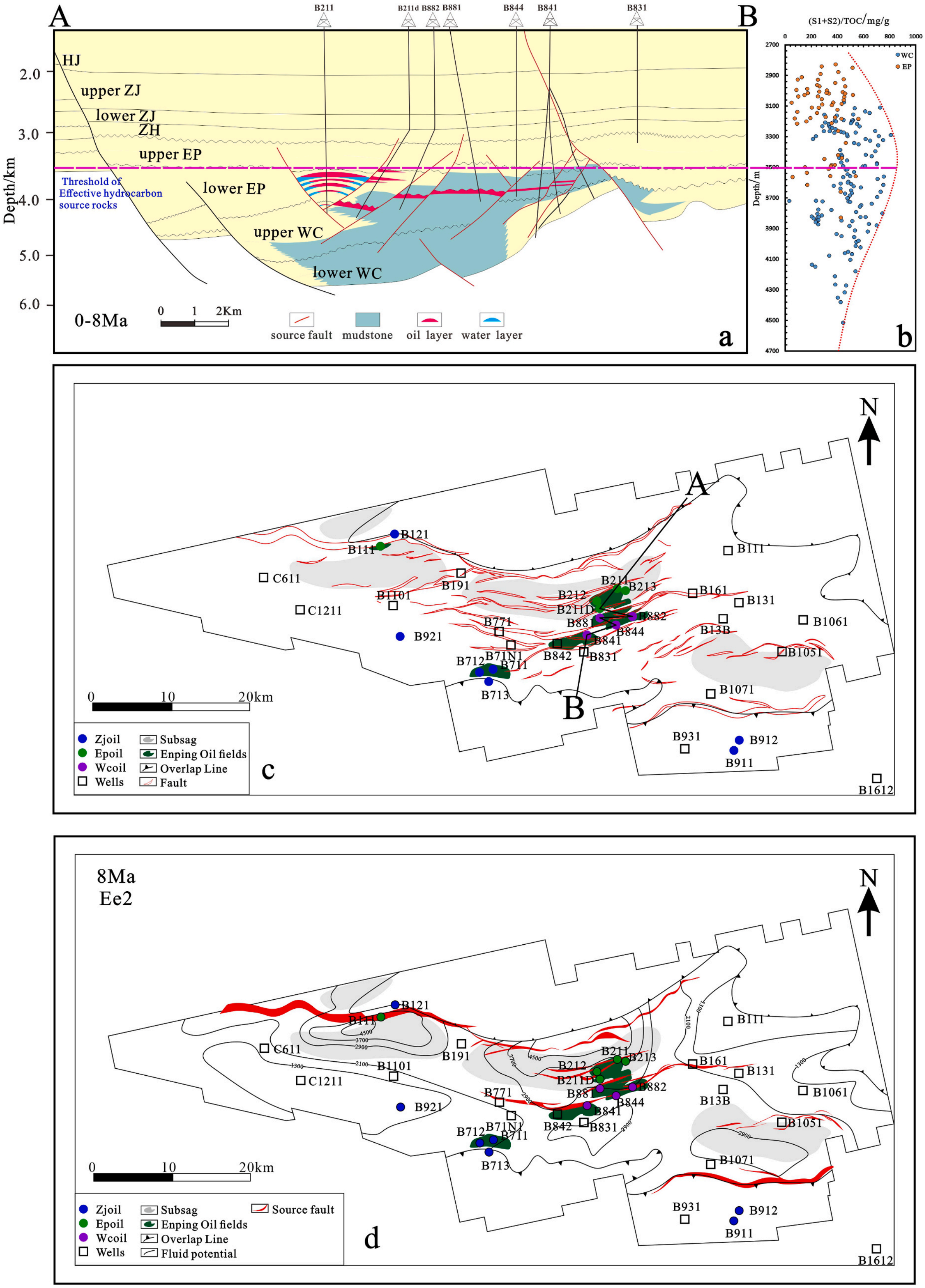

Fig. 14. Discrimination diagram of the source faults in the second accumulation period in the southern Lufeng area. (a) Schematic diagram of the source fracture profile. (b) Statistical chart of the depth corresponding to the hydrocarbon expulsion threshold. (c) Plane distribution of faults in the southern Lufeng area. (d) Plane distribution of source faults in the second accumulation period in the southern Lufeng area.

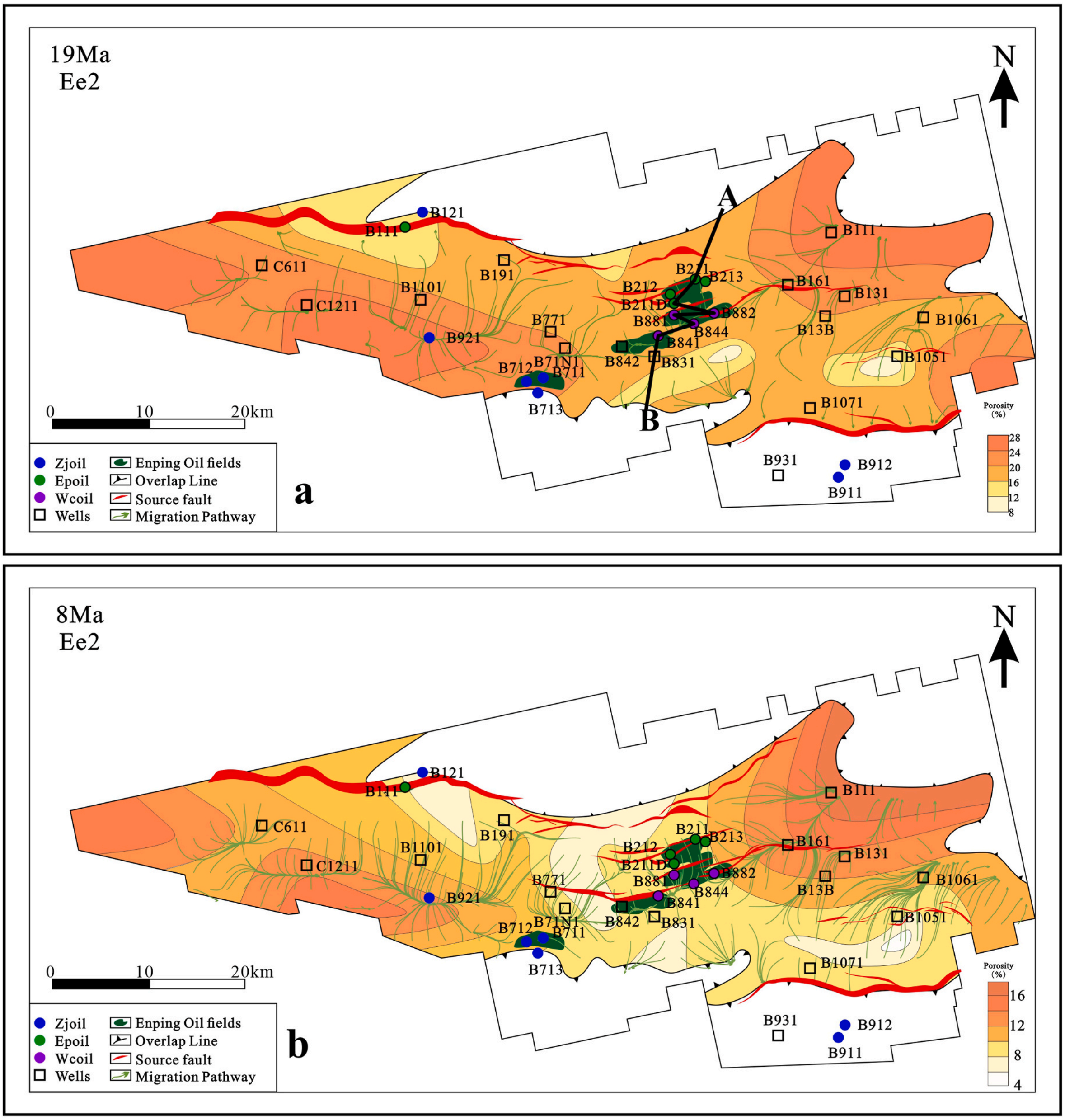

Fig. 15. Plane distribution of the migration system of the lower Enping Formation in the southern Lufeng area for the first (a) and second (b) accumulation periods.

2019) were used to mark the reservoirs on the profile. The oil-source correlation results show three types of source rocks of the Wenchang Formation mainly developed in this area: shallow lacustrine, deep lacustrine, and deep lacustrine–semi-deep lacustrine source rocks. Three main types of crude oil were observed: crude oil from shallow lacustrine source rocks, crude oil from deep lacustrine or deep lacustrine and semi-deep lacustrine source rocks, and mixed-source oil (Fig. 16b).

In the first stage (19–8Ma), the migration mode is a long distance fault–sand–ridge coupling transport system. The distribution of source faults in the plane of the first stage is relatively limited, mainly at the edge of the depression and the uplift zone. In the meantime, however, the relatively shallow depth of burial allows for relatively high porosity in the sandstone reservoir, which facilitates the long-distance transport of hydrocarbons. Therefore, oil and gas generally accumulated at the fault trap and the convergence of structural ridges (Fig. 15a).

In the second stage (8–0 Ma), the migration mode is a near-source fault transport system. At this stage, because of the increase in burial depth and the strengthening of compaction, the porosity of the transverse migration system and the range of the dominant migration system were reduced (areas with porosity greater than 10%). In addition, the range of hydrocarbon expulsion from the source rocks increased, and the range of the source faults of the second accumulation period expanded.

5. Discussion

In terms of the results of the construction of the transport system, the results correspond to the "The migration drainage style" mentioned by the previous authors (Demaison and Huizinga., 1994): where the oil source fracture corresponds to "Vertical migration drainage"; the sandstone transport conductor corresponds to "lateral migration drainage"

In this study, as the burial depth increased, the hydrocarbon expulsion range increased, leading to an increased number of source faults. Simultaneously, the range of the dominant sand body decreased. In addition, the tectonic amplitude and the gathering area of the structural

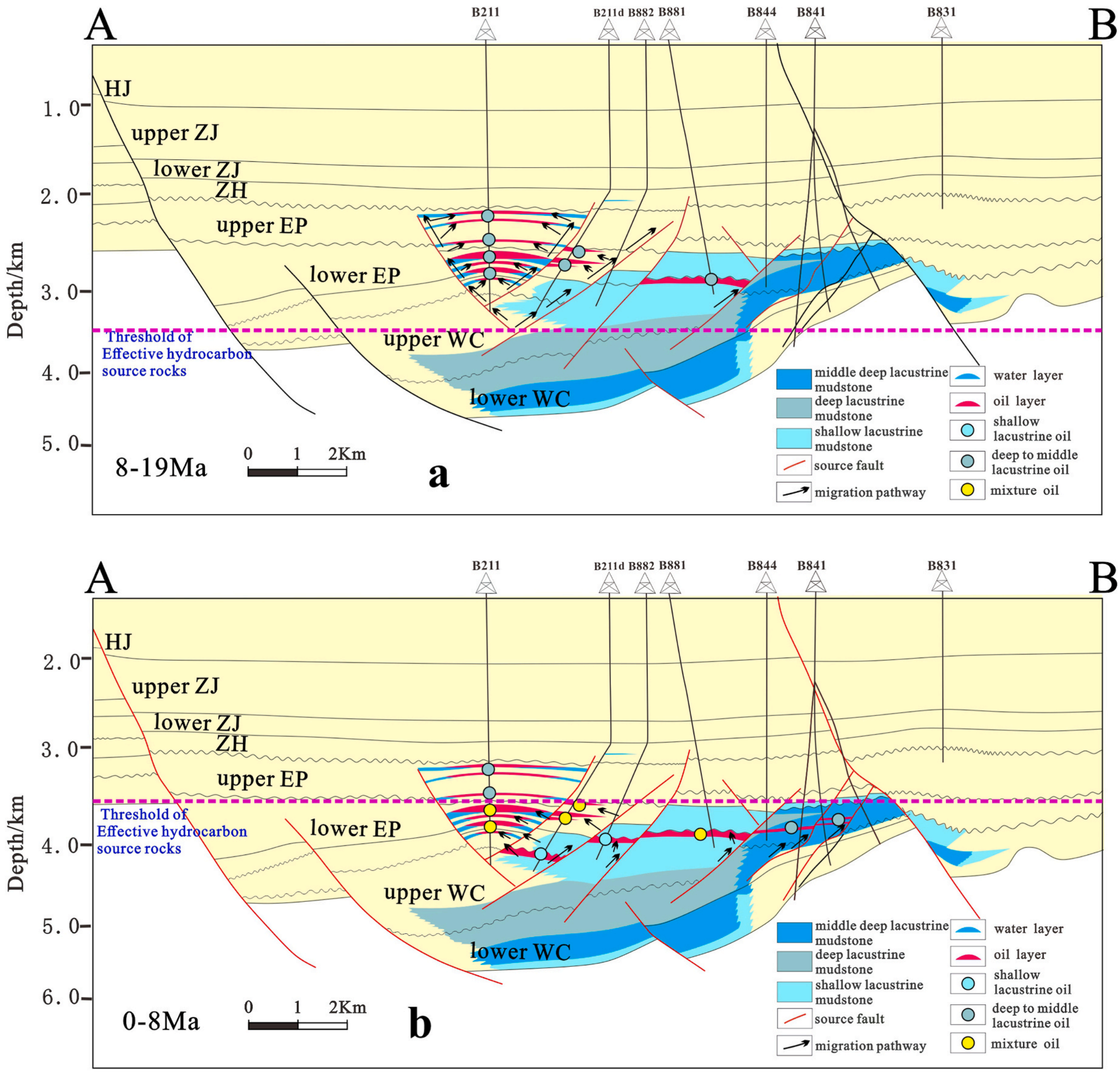

Fig. 16. Section distribution of the migration system of the lower Enping Formation in the southern Lufeng area for the first (a) and second (b) accumulation periods.

ridge reduced with increasing burial depth. Generally, the distribution of source faults determined the lower limit of the accumulation range, whereas the distribution of dominant sand bodies determined the upper limit. When source faults communicated with dominant sand bodies, oil and gas tended to be transported over long distances. In contrast, when source faults communicated with nondominant sand bodies, oil and gas tended to form near-source reservoirs.

Therefore, despite the wide distribution of sand bodies in the first accumulation stage, reservoirs were only formed at local structural highs because of the limitation of the source fault distribution. And the oil and gas in this period were mainly deep lacustrine oils, which formed in the high part of a remote local structure. The oil and gas in the lower Enping Formation mainly accumulated along the source faults in the central uplift belt to the central uplift belt. Structural reservoirs were mainly formed at this time.

In the second stage, although the source fault range was expanded, oil and gas were only charged near the fault because of the reduction of the dominant sand body range., The shallow lacustrine source rocks began to expel a large amount of hydrocarbons. Although the range of hydrocarbon expulsion and source faults were large at this time, the hydrocarbon were not transported to long distances because of the limited transportation capacity of the sand bodies. Thus, the reservoirs mainly formed near the source (Fig. 15b). In the center of the depression, besides some shallow lacustrine oil that formed during this period, a reservoir filled with deep lacustrine oil was observed, such as in B881, which becomes mixed oil under the infiltration of shallow lacustrine crude oil. Deep lacustrine oil was formed by near-source charging of middle and deep lacustrine source rocks in the southern slope area. Structural and lithologic reservoirs mainly formed during this accumulation stage (Fig. 16b).

The favorable areas in each accumulation period were predicted by combining the migration system with the trap distribution. Finally, the traps of the different accumulation periods in the southern Lufeng area were divided into effective traps (favorable traps for accumulation) and ineffective traps (unfavorable traps for accumulation). The effective traps are the structural traps in the dominant sand body along the structural ridge path and the traps in the nondominant sand body near the oil-source fault. Others were considered invalid traps (Fig. 17a and b).

Fig. 17 shows that in the first stage, the traps along the structural ridge path were widely distributed because of the good porosity of the whole area. The traps in the middle and east were small and scattered, mainly structural traps related to faults. The western part is mainly a large anticlinal trap (Fig. 17a).

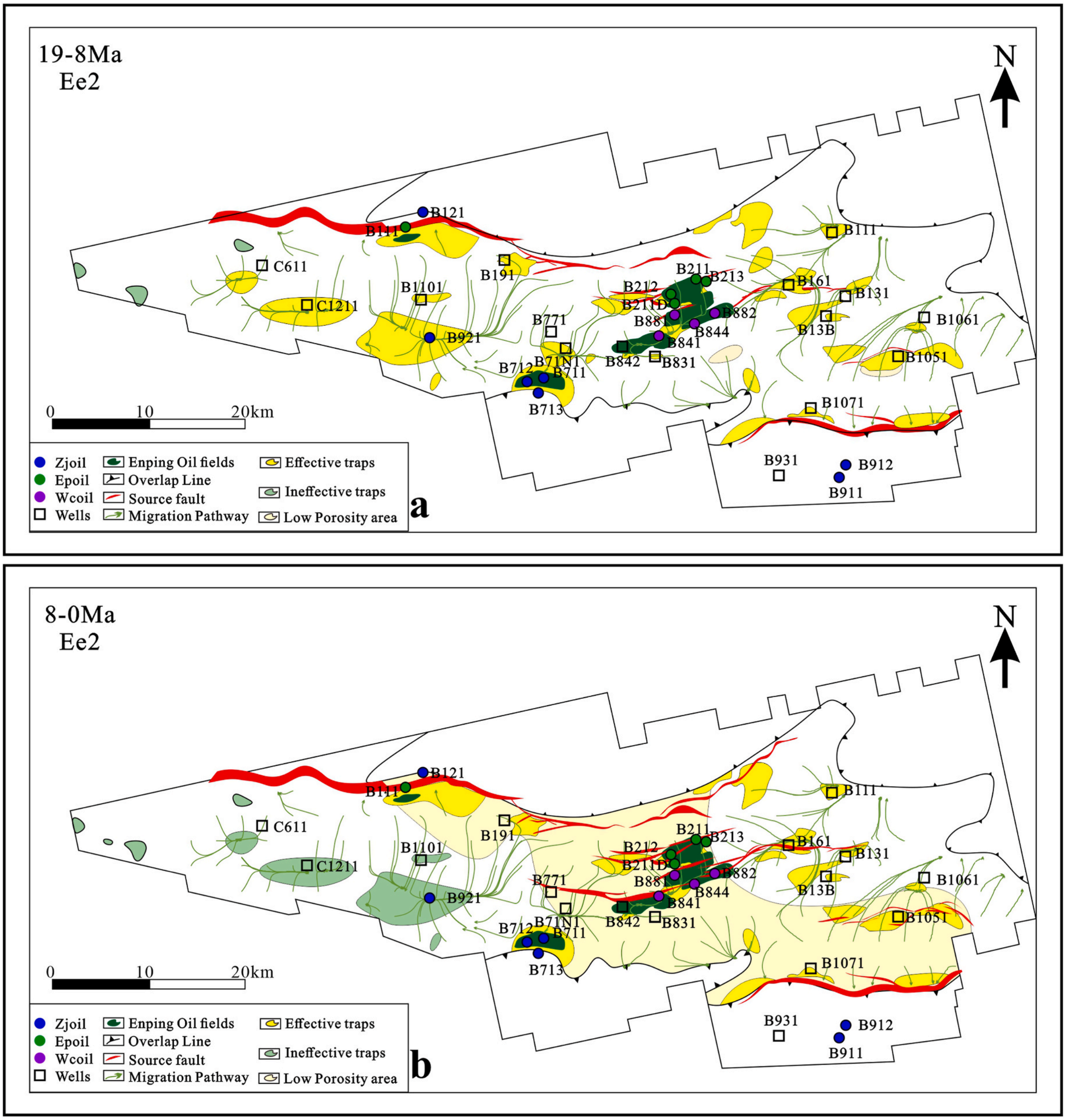

Fig. 17. Prediction of favorable traps in the southern Lufeng area for the first (a) and second (b) accumulation periods.

In the second stage, long-distance migration was limited because of the low porosity in most of the central region. Thus, the main enrichment areas were near the source faults. However, those in the western edge range of the sand body were less associated with source faults, and the migration path did not match with the source fault (the source fault is at the beginning of the migration path). The lack of hydrocarbon migration channels was not conducive to hydrocarbon migration accumulation. Many source faults were observed in the east, and they matched well with the structural ridges. Therefore, long-distance migration conditions were present in the east, and the traps above the migration path are hydrocarbon accumulation areas (Fig. 17b).

According to the current exploration situation and the favorable areas in different accumulation periods, the exploration target can be shifted to the south of the Lufeng area (east area of B713) and to the northern area (north area of B111) to search for structural and lithologic reservoirs.

6. Conclusion

1) Two main stages of hydrocarbon charging were found using fluid inclusions to determine the accumulation period in the southern Lufeng area: early stage (19–8 Ma) and late stage (8–0 Ma).
2) Based on density variation and fluid potential, oil and gas were found to have migrated diversely from the eastern Lufeng 13 depression to the south and west in each accumulation period. In the first stage, the fault–sand–ridge coupling transport system was adopted and structural reservoirs were mainly formed in the high part of the structure. The second stage featured a near-source fault transport system. Structural and lithologic reservoirs were mainly formed near the source faults.
3) According to the current exploration situation and favorable areas observed during different accumulation periods, the next step is to explore lithologic reservoirs in the southern Lufeng area (eastern area of B713) and structural reservoirs in the undeveloped structural traps in the northern area (northern area of B111).

Credit author statement

Hong pang: Conceptualization, Methodology, Kuiyou Ma: Methodology, Visualization.Shengmin Huang: Data curation, Writing – original draft. Formal Analysis, Hongbo Li: Software, Validation, Resources.Lili Zhang: Software, Validation, Resources.Sa Yu: Software, Validation, Resources

Declaration of competing interest

The authors declare that they have no known competing financial interests or personal relationships that could have appeared to influence the work reported in this paper.

Data availability

The data that has been used is confidential.

Acknowledgements

This study was supported by the Major National R&D Projects of China (Grant No. 2016ZX05024-004) and research project of CNOOC (Shenzhen) (Grant No. SCKY-2020-SZ-21) We are grateful to CNOOC for providing experimental samples and permitting the publication of this research.

Appendices.

Table A
Logging interpretation porosity statistics

Well	Formation	Depth/m	Porosity/%	Permeability/mD
B721	ZJ	2491.75	19	871.048
B721	ZJ	2499	21.7	1576.436
B841	ZJ	2432.2	22.6	3255.899
B841	WC	3648.5	9.4	8.353
B841	WC	3663.5	8.5	2.175
B841	WC	3688.2	10.5	3.903
B841	WC	3694.25	12.4	12.41
B841	WC	3789.5	10.2	2.658
B841	WC	3845.5	8.2	2.158
B841	WC	3859	9	9.104
B841	WC	3893.85	11.9	6.655
B842	WC	3810.9	13.2	42.5
B842	WC	3837	14.3	101.6
B843	WC	3674.2	14.3	53.453
B843	WC	3680.8	13.8	48.881
B843	WC	3723.75	11.1	4.905
B843	WC	3726.1	10.7	2.563
B843	WC	3730.3	13.9	37.058
B881	WC	3693.75	12	9.856
B881	WC	3699	14.9	43.743
B881	WC	3717.5	13.9	103.787
B881	WC	3729.75	14.3	22.217
B881	WC	3747.3	11.7	8.232
B1051	WC	3285.2	16.2	415.23
B1051	WC	3296.55	16.5	522.47
B1051	WC	3394	13.9	71.343
B1051	WC	3405.5	15	165.65
B1051	WC	3438.35	13.2	41.739
B1051	WC	3677.3	13.6	56.7
B1051	WC	3686.1	13.7	61.2
B1051	WC	3694.2	13.6	56.7
B1061	EP	2962.5	19.3	134.6
B1061	EP	2977.5	18.9	108.2
B1061	EP	2988.3	20.3	255.8
B1061	EP	2996.55	17.2	38.7
B1061	EP	3426.1	18.8	46.3
B1071	EP	3259.5	12.5	7.5
B1071	EP	3268.5	12.8	5.3
B1071	WC	3305.5	11.5	3.5
B1071	WC	3327	10.2	1.2
B1071	WC	3348.5	10.3	1.3
B1071	WC	3523	10.1	1.1
B1071	WC	3542	10.1	1.1
B111	ZJ	2523.15	22.225	2100.04
B111	ZJ	2588.2	14.0445	30.9729
B111	ZJ	2641.8	16.8346	111.817
B111	ZJ	2656.4	15.5186	76.4509
B111	ZJ	2669.15	17.3616	231.731
B111	ZJ	2686.25	15.8392	275.251
B111	ZH	2704.65	17.094	648.445
B111	ZH	2742.4	14.7125	123.392
B111	ZH	2783.65	14.8171	63.386
B111	ZH	2796.6	12.7401	33.3803
B111	ZH	2810.85	14.4668	75.6326

(*continued on next page*)

Table A (*continued*)

Well	Formation	Depth/m	Porosity/%	Permeability/mD
B111	ZH	2824.75	13.3365	66.6311
B111	ZH	2843.35	12.6515	65.6057
B111	ZH	2861.55	14.6986	78.1153
B111	ZH	2868.95	13.1052	31.3703
B111	EP	2892	12.6888	29.8104
B111	EP	2925.9	12.7636	39.4639
B111	EP	2958.9	12.9124	33.1121
B111	EP	2978.95	11.482	15.9353
B213	EP	3444.55	14	32.1
B213	EP	3553.75	17.4	217.3
B213	EP	3561.15	16	98.9
B213	EP	3584.25	14.5	42.5
B221	EP	3443.5	14.033	28.767
B331	WC	2910.05	14	33
B361	WC	2922.4	25.053	13664.99
B361	WC	2992.15	18.381	330.102
B212	EP	3456.7	18.7	57
B212	EP	3590.3	17.4	1.5
B212	EP	3613.35	12.9	10.7
B212	EP	3705.55	14.3	15.4
B212	EP	3736.9	14.8	19.6
B211d	EP	3432.55	17.6	46.8
B211d	EP	3445.45	17.7	46.6
B211d	EP	3504	16.7	36.4
B211d	EP	3514.1	17.5	44.8
B211d	EP	3522.65	16.8	36.9
B211d	EP	3539.15	16.5	34.6
B71N1	ZJ	2460	18.8	274
B71N1	ZJ	2534	22.5	342
B71N1	ZJ	2541.75	16.8	96
B71N1	ZJ	2575.5	17.4	140
B71N1	ZJ	2622.15	23.4	558
B71N1	ZJ	2714.9	18	259
B841	ZJ	2441.8	21.6	1298.7
B841	WC	3674	10.5	1.6
B841	WC	3680.05	10	1.2
B841	WC	3713.7	12.4	2.6
B841	WC	3745.35	13.4	3.2
B841	WC	3760	11.4	2
B841	WC	3769.5	10.7	1.7
B841	WC	3844.9	10	1.4
B841	ZJ	2457.65	22.7	1253.2
B841	ZJ	2475.85	24.6	3906.7
B841	WC	3728.25	11.9	0.3
B841	WC	3745.85	12.2	0.3
B841	WC	3890.1	12.4	0.3
B844	ZJ	2453.5	22.9	2485.8
B844	ZH	2671	18.6	510.4
B844	ZH	2719.5	19.1	580.1
B844	WC	3899.25	13.6	1.8
B882	ZH	2784.6	18	73.8
B882	EP	3082.75	18.7	112.6
B121	ZJ	2393.1	19.4	1616.9
B841	WC	3909.55	12.2	11.258
B841	WC	3914.7	11.7	5.896
B841	WC	3919.5	11	6.128
B841	WC	3927.45	11.8	10.613
B841	WC	3933.15	14.1	34.455
B841	WC	3940.2	11.3	10.924
B841	WC	3949.1	11.1	6.27
B841	WC	3956.5	12.4	11.406
B841	WC	3965.15	11.8	5.795
B841	WC	3978	10.8	4.348
B841	WC	3995.05	10.7	3.753
B841	WC	4005.6	11.6	8.551
B841	WC	4016	10.9	3.181
B841	WC	4028.25	8.7	2.962
B841	WC	4035.5	12.3	35.079
B841	WC	4044.2	10	5.923
B843	WC	4000.45	10.1	14.952
B843	WC	4007.7	7.5	3.347
B843	WC	4015.8	7.1	3.824
B843	WC	4058.9	10.4	13.676
B843	WC	4092.5	7.7	4.803
B843	WC	4167	11.5	24.193
B843	WC	4172.7	10.7	20.251

(*continued on next page*)

Table A (*continued*)

Well	Formation	Depth/m	Porosity/%	Permeability/mD
B843	**WC**	**4205**	**5.6**	**0.98**
B843	**WC**	**4209.5**	**7.3**	**6.262**
B843	**WC**	**4215.5**	**9.7**	**11.109**
B843	**WC**	**4223.4**	**8.2**	**6.784**
B843	**WC**	**4237.65**	**10.5**	**19.167**
B881	**WC**	**4059.15**	**9.6**	**3.548**
B221	**EP**	**3971.5**	**10.852**	**4.564**
B221	**EP**	**3977.6**	**11.167**	**6.586**
B221	**EP**	**3989.6**	**10.735**	**4.511**
B841	**WC**	**3970.55**	**11.7**	**2.2**
B841	**WC**	**3981.95**	**10.8**	**1.7**
B841	**WC**	**3987.1**	**11.9**	**2.2**
B841	**WC**	**4018.9**	**14.2**	**10**
B841	**WC**	**4028.7**	**13.6**	**4**
B841	**WC**	**4036.25**	**13.1**	**3**
B841	**WC**	**4042.5**	**10.9**	**1.7**
B841	**WC**	**4056**	**10.6**	**1.6**
B841	**WC**	**4069.5**	**11.4**	**2**
B841	**WC**	**4081.85**	**10.3**	**1.5**
B841	**WC**	**4098.4**	**11.9**	**2.3**
B841	**WC**	**4109.4**	**10.7**	**1.7**
B841	**WC**	**4117**	**11.7**	**2.1**
B841	**WC**	**4338.9**	**12.5**	**2.5**
B841	**WC**	**3901.95**	**10.9**	**0.1**
B841	**WC**	**3907.5**	**9.8**	**0.1**
B844	**WC**	**4048.85**	**12.3**	**0.5**
B842	**WC**	**3929.7**	**13.9**	**3.8**
B842	**WC**	**3947.25**	**14.9**	**20.6**
B842	**WC**	**3979.3**	**15.9**	**38.5**
B842	**WC**	**4039.5**	**14**	**10.8**

Appendices B

Table B
Statistics of the hydrocarbon expulsion index of the source rocks

Well	Formation	Depth	(S1+S2)	TOC	(S1+S2) /TOC × 100 (mg/g)
B191	**EP**	**3532**	**0.05**	**0.03**	**166.6666667**
B191	**EP**	**3559**	**0.08**	**0.14**	**57.14285714**
B191	**EP**	**3610**	**0.17**	**0.1**	**170**
B211	**EP**	**2967**	**1.58**	**0.6**	**263.3333333**
B841	**EP**	**3006**	**2.47**	**0.56**	**441.0714286**
B841	**EP**	**3090**	**1.79**	**0.5**	**358**
B841	**EP**	**3207**	**2.1**	**0.59**	**355.9322034**
B1071	**EP**	**2820**	**4.44**	**1.15**	**386.0869565**
B1071	**EP**	**3020**	**4.78**	**0.92**	**519.5652174**
B1071	**EP**	**3200**	**4.53**	**0.9**	**503.3333333**
B2731	**EP**	**2705**	**0.53**	**0.07**	**757.1428571**
B2731	**EP**	**2762**	**0.24**	**0.04**	**600**
B2731	**EP**	**2864**	**0.6**	**0.1**	**600**
B2731	**EP**	**2966**	**0.57**	**0.46**	**123.9130435**
B2731	**EP**	**3008**	**0.42**	**0.08**	**525**
B2731	**EP**	**3056**	**3.87**	**1.6**	**241.875**
B711	**EP**	**3040**	**2.19**	**0.78**	**280.7692308**
B711	**EP**	**3130**	**1.15**	**0.47**	**244.6808511**
B711	**EP**	**2911.4**	**0.6**	**0.47**	**127.6595745**
B711	**EP**	**2995**	**0.59**	**0.68**	**86.76470588**
B711	**EP**	**3037.5**	**0.94**	**0.93**	**101.0752688**
B711	**EP**	**3077.5**	**0.25**	**0.5**	**50**
B711	**EP**	**3137.5**	**0.45**	**0.48**	**93.75**
B711	**EP**	**3177.5**	**0.31**	**0.42**	**73.80952381**
B711	**EP**	**3215**	**0.32**	**0.35**	**91.42857143**
B821	**EP**	**2924.8**	**77.25**	**17.23**	**448.3459083**
B821	**EP**	**2928**	**3.34**	**1.33**	**251.1278195**
B821	**EP**	**2987**	**0.83**	**0.49**	**169.3877551**
B821	**EP**	**3005.6**	**0.55**	**0.21**	**261.9047619**
B821	**EP**	**3110**	**2.41**	**1.18**	**204.2372881**
B821	**EP**	**3200**	**2.28**	**1.4**	**162.8571429**
B191	**EP**	**3798**	**1.15**	**0.76**	**151.3157895**
B1101	**EP**	**3165**	**4.13**	**1.33**	**310.5263158**
B1102	**EP**	**3336**	**51.27**	**11.04**	**464.4021739**

(*continued on next page*)

Table B (*continued*)

Well	Formation	Depth	(S1+S2)	TOC	(S1+S2) /TOC × 100 (mg/g)
B1103	**EP**	**3435**	**3.61**	**0.83**	**434.939759**
B1104	**EP**	**3479**	**2.4**	**0.63**	**380.952381**
B212	**EP**	**3441**	**2.73**	**0.91**	**300**
B213	**EP**	**2946**	**2.53**	**0.66**	**383.3333333**
B213	**EP**	**3057**	**2.56**	**0.57**	**449.122807**
B213	**EP**	**3180**	**2.03**	**0.47**	**431.9148936**
B213	**EP**	**3510**	**2.53**	**0.76**	**332.8947368**
B213	**EP**	**3555**	**3.29**	**0.61**	**539.3442623**
B213	**EP**	**3657**	**3.57**	**0.84**	**425**
B213	**EP**	**3822**	**4.14**	**0.97**	**426.8041237**
B213	**EP**	**3557.6**	**0.38**	**0.11**	**345.4545455**
B211d	**EP**	**3120**	**3.64**	**0.91**	**400**
B211d	**EP**	**3414**	**3.81**	**0.94**	**405.3191489**
B211d	**EP**	**3480**	**2.52**	**0.71**	**354.9295775**
B331	**EP**	**3015**	**9.97**	**2.97**	**335.6902357**
B331	**EP**	**3037**	**31.08**	**6.87**	**452.4017467**
B331	**EP**	**3085**	**5.26**	**1.85**	**284.3243243**
B331	**EP**	**3174**	**2.36**	**1.22**	**193.442623**
B341	**EP**	**3381**	**2.87**	**0.9**	**318.8888889**
B341	**EP**	**3516**	**2.47**	**0.61**	**404.9180328**
B344	**EP**	**2971**	**146.19**	**31.78**	**460.0062933**
B981	**EP**	**2870**	**26.45**	**6.5**	**406.9230769**
B981	**EP**	**3105**	**3.12**	**1.21**	**257.8512397**
B981	**EP**	**3177**	**3.42**	**0.61**	**560.6557377**
B1061	**EP**	**3011**	**5.85**	**1.85**	**316.2162162**
B1061	**EP**	**3071**	**4.3**	**1.17**	**367.5213675**
B831	**EP**	**3037**	**3.61**	**1.44**	**250.6944444**

Appendices C

Table C
Parameter selection for burial history simulation

Age (Ma)	Terrestrial heat flow value (mW/m^2)	Surface temperature (°C)	Paleodepth (m)
0	50	20	10
0.08	50	20	10
7.95	52	20	10
11.83	51	20	10
15.42	52	20	10
19.2	56	20	10
22.8	58	20	10
26.4	60	20	10
30	63	20	10
33.6	64	20	10
37.2	63	20	10
44.4	65	20	10

Appendices D

ASTM D5002-2013

Apparatus.

1. Digital Density Analyzer—A digital analyzer consisting of a U-shaped, oscillating sample tube and a system for electronic excitation, frequency counting, and display.

2. Circulating Constant-Temperature Bath, capable of maintaining the temperature of the circulating liquid constant to 60.05 °C in the desired range. Temperature control can be maintained as part of the density analyzer instrument package.

3. Syringes, at least 2 mL in volume with a tip or an adapter tip that will fit the inlet of the density analyzer.

4. Flow-Through or Pressure Adapter, for use as an alternative means of introducing the sample into the density meter.

5. Thermometer, calibrated and graduated to 0.1 °C, and a thermometer holder that can be attached to the instrument for setting and observing the test temperature. In calibrating the thermometer, the ice point and bore corrections should be estimated to the nearest 0.05 °C. Precise setting and

control of the test temperature in the sample tube is extremely important. An error of 0.1 °C can result in a change in density of one in the fourth significant figure.

Reagents and Materials

1. Water, redistilled, freshly boiled and cooled reagent water for use as a primary calibration standard.
2. Acetone, for flushing and drying the sample tube. (Warning: Extremely flammable.)
3. Petroleum Naphtha,6 for flushing viscous petroleum samples from the sample tube. (Warning: Extremely flammable.)
4. n-Nonane, n-tridecane or cyclohexane, 99% purity or better,

Preparation of Apparatus

Set up the density analyzer and constant temperature bath following the manufacturer's instructions. Adjust the bath or internal temperature control so that the desired test temperature is established and maintained in the sample compartment of the analyzer. Calibrate the instrument at the same temperature at which the density of the sample is to be measured.

Test method

Approximately 0.7 mL of crude oil sample is introduced into an oscillating sample tube and the change in oscillating frequency caused by the change in the mass of the tube is used in conjunction with calibration data to determine the density of the sample.

Appendices E

GB/T29172-2012

Core sample volume determination

Apparatus.

1. A single pan electronic analytical balance with an accuracy of 0.01g.
2. The plunger sample can be placed horizontally in a container of suitable size so that it is completely submerged and the plunger sample does not touch the walls of the container.The plunger sample is placed horizontally in the container so that it is fully submerged and the plunger sample does not touch the walls of the container.
3. The container is filled with mercury so that the plunger sample is completely submerged.
4. Adjustable, end-branching holder with reference mark.
5. Thermometer.

Test method. The surface of the sample is sealed with paint and then submerged in mercury, which is weighed and the volume is obtained from the density of the mercury at the measurement temperature ("Archimedes" principle).

Pore volume determination

Apparatus.

1. An analytical balance accurate to 1 mg.
2. Suitable containers for degassed liquids under vacuum
3. Vacuum dryer and pressure saturation unit.
4. A suitable vacuum source capable of keeping the pressure below 13.3 Pa (0.1 mmHg).
5. Known density, filtered, low viscosity, low vapour pressure liquids for saturated rock samples. Commonly used liquids include: brine, refined laboratory oils, and sunflower toluene.
6. Suitable containers for saturated rock samples immersed in degassed liquids.

Test method.

1. Weigh the mass of a clean, dry rock sample. Before weighing the dry rock sample, it should be dried with a drying agent such as CCl2 or silica gel.

2. Place the weighed dry sample in a container (vacuum dryer and pressure saturator) and evacuate for approximately 8 h. While evacuating, CO2 can be injected to remove the air adsorbed on the rock surface. A gas with better solubility in liquids is generally used to replace the adsorbed gas, such as O2 gas. For low permeability samples, several cycles of vacuum and CO2 injection are repeated, and in dense samples, the longer the CO2 contact time is in order to drive out N2, the longer the vacuum cycle will take. For very low permeability samples, the vacuuming time should be extended to 12h–18h (one day and night).

3. Fluids used to saturate clean rock samples should be free of dissolved air. The fluid should therefore be degassed before being injected into the rock sample. Great care should be taken during handling to avoid contact of the degassed liquid with air. Hydrocarbons are strong wetting fluids compared to brine and are chosen as the saturating fluid without brine if only porosity determination is required and no other experiments need to be performed.

4. The degassed liquid is injected into a vacuum vessel containing the rock sample to saturate it. After the sample is completely submerged in the liquid, the vacuum is continued for 30 min to 1h.

5. The best way is to pressurise the liquid around the sample to 13,800 kPa-20,700 kPa (2000psi-3000psi) for at least 4h to ensure complete saturation.

6. Pressurisation saturates the fluid into poorly connected pore spaces or pores where spontaneous aspiration has not occurred. The sample is then removed from the saturation vessel and the mass of the sample submerged in the saturated liquid is weighed. This mass was subtracted from the mass of the dry rock sample and divided by the density of the fluid, which then gave the actual volume of the pore space.

7. Once the pore volume and the sample volume are obtained, the porosity of the sample is calculated by dividing the two.

Core permeability determination

Apparatus. Full Diameter Radial Flow Permeability Meter.

Test method. The core is placed on a rubber gasket attached to the lower floating plate so that the central hole in the core is aligned with the small hole in the gasket. If the two ends are not parallel, as the piston pressure increases, the lower floating plate automatically adjusts its position so that it fits snugly into the end face of the core. Therefor increasing the piston pressure detects whether the core ends are sealed to the rubber gasket. As the pressure increases, if the flow rate decreases, this indicates a leak. This is repeated until the flow rate is stable.

Appendices F

SYT 5120-1997

Apparatus

1. Gas chromatograph: with capillary column split or splitless injection system, programmed temperature rise and flame ionisation detector unit.
2. Data processing unit (or with recorder).
3. Refrigerator.

Reagents and Materials

1. Hexane or isooctane
2. Chromatographic specimens: n-alkane specimens containing any number of carbons in the range C13 to C40.
3. Chromatographic column: flexible quartz capillary column, stationary phase is methyl silicone or methyl phenyl silicone, column length 20–30m, inner diameter 0.20–0.32 mm; maximum operating temperature not less than 300 °C.
4. Micro syringes: 1L,10L.
5. Sample bottle with cap. Volume 0.5–1.01 mL.
6. Nitrogen or ammonia: purity not less than 99.99%.
7. Hydrogen: purity not less than 99.9%.

Preparation of Apparatus

1. Saturated hydrocarbon fractions from rock chloroform extracts or crude oil separated by family fractions, stored in a refrigerator or in a cool place
2. For split injection, dilute the sample with an appropriate amount of n-hexane; for non-split injection, dilute the sample with an appropriate amount of isooctane.

Test method

1. Pass in gas and check the gas circuit of the analysis system to eliminate leaks and blockages.
2. Start the instrument according to the operating procedures of each instrument
3. Ignite the flame and check the stability of the chromatographic baseline during the programmed temperature rise.

4. Choose between split or non-split injection methods and injection volumes depending on the sample volume.
5. The sample is injected with a micro syringe while the program is started to warm up and the harmonic plots are recorded and data collected.

Appendices:

SYT 6385-1999

Apparatus

1. CMS series of automatic core analyzers and other similar core overburden pore penetration meters.
2. Ammonia porosimeter: relative error less than or equal to 0.5%.
3. Atmospheric pressure gauge: Class 0.4.
4. Vernier calipers: 0.02 mm index value.

Test method

1. Turn on the power and gas supply of the CMS core analyzer and warm up the machine for 30 min.
2. Set each pressure regulator to the required pressure in the order as required by the instrument.
3. Start the test program and run the self-test or leak test program.
4. Run the sample test program, first enter the atmospheric pressure and experimental temperature data under the test environment, then enter the number of test samples to be analyzed and their base parameters.
5. The maximum experimental envelope pressure is selected by one-half of the overlying rock pressure and is divided into 4 to 8 pressure points below.
6. The samples to be determined are loaded in the sample carousel in sequence for testing.
7. The computer automatically collects the stored data and derives the triaxial porosity and permeability.
8. When the test is complete, the gas source and the instrument power supply are switched off in sequence.
9. Instrument calibration: After every 500 rock samples have been tested, the instrument is calibrated with a standard volume block and a pore penetration standard substance, with an envelope pressure of not more than 5.515 MPa.

References

Berg, R.R., 1975. Capillary pressures in stratigraphic traps. AAPG (Am. Assoc. Pet. Geol.) Bull. 59. https://doi:10.1306/83d91ef7-16c7-11d7-8645000102c1865d.

Galeazzi, J.S., 1998. Structural and stratigraphic evolution of the western Malvinas basin, Argentina. AAPG (Am. Assoc. Pet. Geol.) Bull. 82 (4), 596–636. https://doi:10.1306/1d9bc5c5-172d-11d7-8645000102c1865d.

Gibson, R.G., 1994. Fault-zone Seals in Siliciclastic Strata of the Columbus Basin, Offshore Trinidad. AAPG Bulletin 78. https://doi:10.1306/a25feca7-171b-11d7-8645000102c1865d.

Hunt, J.M., 1990. Generation and migration of petroleum from abnormally pressured fluid compartments. AAPG (Am. Assoc. Pet. Geol.) Bull. 74. https://doi:10.1306/0c9b21eb-1710-11d7-8645000102c1865d.

Smith, D.A., 1980. Sealing and nonsealing faults in Louisiana gulf coast salt basin. AAPG (Am. Assoc. Pet. Geol.) Bull. 64. https://doi:10.1306/2f918946-16ce-11d7-8645000102c1865d.

Seifert, W.K., Moldowan, J.M., 1978. Applications of steranes, terpanes and monoaromatics to the maturation, migration and source of crude oils. Geochem. Cosmochim. Acta 42, 77–95. https://doi:10.1016/0016-7037(78)90219-3.

Leythaeuser, D., Schwark, L., Keuser, C., 2000. Geological conditions and geochemical effects of secondary petroleum migration and accumulation. Mar. Petrol. Geol. 17 (7), 857–859. https://doi:10.1016/S0264-8172(00)00010-6.

Bense, V.F., Van den Berg, E.H., Van Balen, R.T., 2003. Deformation mechanisms and hydraulic properties of fault zones in unconsolidated sediments; the Roer Valley Rift System, The Netherlands. Hydrogeol. J. 11 (3), 319–332. https://doi:10.1007/s10040-003-0262-8.

Bethke, J., Reed, 1991. Long-range petroleum migration in the Illinois basin. AAPG (Am. Assoc. Pet. Geol.) Bull. 75. https://doi:10.1306/0c9b2899-1710-11d7-8645000102c1865d.

Billi, A., Salvini, F., Storti, F., 2003. The damage zone-fault core transition in carbonate rocks: implications for fault growth, structure and permeability[J]. J. Struct. Geol. 25 (11), 1779–1794.

Bourdet, J., Kempton, R.H., Dyja-Person, V., 2019. Constraining the timing and evolution of hydrocarbon migration in the Bight Basin. Mar. Petrol. Geol. https://doi:104193.10.1016/j.marpetgeo.2019.104193.

Chandler, M., A., G., Kocurek., D., J., Goggin, 1989. Effects of stratigraphic heterogeneity on permeability in eolian sandstone sequence, Page Sandstone, northern Arizona. AAPG (Am. Assoc. Pet. Geol.) Bull. 73, 658–668.

Chen, J., Ma, K., Pang, X., Yang, H., 2020. Secondary migration of hydrocarbons in Ordovician carbonate reservoirs in the Lunnan area, Tarim Basin. J. Petrol. Sci. Eng. 188. https://doi:10.1016/j.petrol.2020.106962.

Chen, Z., Qiao, R., Li, C., Wang, D., Gao, Y., 2022. Hydrocarbon generation potential and model of the deep lacustrine source rocks in the Dongying Depression, Bohai Bay Basin. Mar. Petrol. Geol. 105656. https://doi:10.1016/j.marpetgeo.2022.105656.

Dai, Y., Niu, Z., Wang, X., Wang, X., Xiao, Z., Zhang, K., Zhao, X., 2019. Differences of hydrocarbon enrichment regularities and their main controlling factors between Paleogene and Neogene in Lufeng sag, Pearl River Mouth Basin. ACTA PETROLE SNNICA 40 (1), 41–52. https://doi:10.7623/syxb2019S1004.

Demaison, G., Huizinga, B.J., 1994. Genetic classification of petroleum systems using three factors: charge, migration and entrapment. AAPG Mem 60, 73–92.

England, W.A., Mackenzie S., A., Mann, D.M., 1987. The movement and entrapment of petroleum fluids in the subsurface. J. Geol. Soc. 144 (2), 327–347. https://doi:10.1144/gsjgs.144.2.0327.

Ge, J., Zhu, X., Pan, R., 2015. A quantitative porosity evolution model of sandstone for WenchangFormation in Huizhou depression, Pearl River Mouth basin: a case study for braided fluvial delta reservoir of HZ-A area [J]. Acta Sedimentol. Sin. 33 (1), 183–193.

Ge, J., Zhu, X., Lei, Y., Yu, F., 2021. Tectono- sedimentary development of multiphase rift basins: an example of the Lufeng Depression. Earth Sci. Front. 28 (1), 77–89. https://doi:10.13745/j.esf.sf.2020.5.9.

Hao, F., Zou, H., Fang, Y., Zeng, Z., 2004. Overpressure-fault controlled fluid flow and episodic hydrocarbon accumulation. Acta Pet. Sin. 25 (6), 38–47.

Hooper, E.C.D., 1991. Fluid migration along growth faults in compacting sediments. J. Petrol. Geol. 14, 161–180. https://doi.org/10.1111/j.1747-5457.1991.tb00360.x.

Horstad, I., Larter, S.R., Mills, N., 1995. Migration of hydrocarbons in the Tampen Spur area, Norwegian North Sea: a reservoir geochemical evaluation. Geological Society, London, Special Publications 86 (1), 159–183. https://doi:10.1144/gsl.sp.1995.086.0.

Hubbert, M.K., 1953. Entrapment of petroleum under hydrodynamic conditions. AAPG (Am. Assoc. Pet. Geol.) Bull. 37 (8), 1954–2026. https://doi:10.1306/5CEADD61-16BB-11D7-8645000102C1865D.

Jiang, Y., Liu, J., Li, X., 2011. Actual hydrocarbon migration paths based on ridge-like structures analysis and geochemical indicators tracking : a case study of puwei area of dongpu depression. Earth Sci. 36 (3), 521–529.

Karlsen, D.A., Skeie, J.E., 2006. Petroleum migration, faults and overpressure, part I: calibrating basin modelling using petroleum in traps - a review. J. Petrol. Geol. 29 (3), 227–256. https://doi:10.1111/j.1747-5457.2006.00227.x.

Knipe, R.J., 1992. Faulting Processes and Fault Seal. Structural and Tectonic Modelling and its Application to Petroleum Geology, pp. 325–342. https://doi:10.1016/b978-0-444-88607-1.50027-9.

Larter, S.R., Bowler, B., Li, M.F.J., 1996. Molecular indicators of secondary oil migration distances. Nature 383 (6601), 593–597. https://doi:10.1038/383593a0.

Li, L., Zhang, X.T., Xu, C.Q., Zhang, Z., Liu, T., 2019. Neogene hydrocarbons distribution characteristics and"ridge-fault " joint control accumulation mode in western Bozhong sag, Bohai sea. China Offshore Oil Gas 31 (4), 27–35. https://doi:10.11935/j.issn.1673-1506.2019.04.004.

Lin, H., Liu, P., Wang, X., 2021. Influences of structural transformation on source-to-sink system during the depositional period of Wenchang Formation of Eocene in the ZhuI depression. Geotect. Metallogenia 45 (1), 188–200. https://doi: 10.16539/j.ddgzyckx.2021.01.017.

Liu, N., Qiu, N., Chang, J., 2017. Hydrocarbon migration and accumulation of the suqiao buried-hill zone in wen'an slope, jizhong subbasin, Bohai Bay Basin, China. Mar. Petrol. Geol. 86, 512–525. https://doi:10.1016/j.marpetgeo.2017.05.040.

Luan, G., Azmy, K., Dong, C., 2021. Fault-controlled carbonate cementation: a case study from Eocene turbidite-delta sandstones (Dongying Depression) and implication for hydrocarbon migration. Mar. Petrol. Geol. 129, 105000. https://doi:10.1016/j.marpetgeo.2021.105000.

Luo, X., Lei, Y., Zhang, L., 2012. Characterization of carrier formation for hydrocarbon migration: concepts and approaches. ACTA PETROLE SINICA 3 (33), 428–436. CNKI:SUN:SYXB.0.2012-03-012.

Luo, X., Sun, Y., Wang, L., Xiao, A., Ma, L., Zhang, X., Wang, Z., Song, C., 2013. Dynamics of hydrocarbon accumulation in the west section of the northern margin of the Qaidam Basin, NW China. Petrol. Explor. Dev. 40 (2), 170–182. https://doi:10.1016/S1876-3804(13)60020-8.

Luo, X., Zhang, L., Lei, Y., Cheng, M., Shi, H., Cao, B., 2020, 41(03). In: Heterogeneity of Clastic Carrier Bed and Hydrocarbon Migration and Accumulation, pp. 253–272. https://doi:10.7623/syxb202003001.

Ma, M., Qi, J., Zhang, Y., 2019. An analysis of subsidence characteristics and affecting factors in the Pearl River Mouth Basin in Cenozoic. In: Geology in China, pp. 269–289. https://doi:CNKI:SUN:DIZI.0.2019-02-006.

Narr, W., 1991. Fracture density in the deep subsurface: techniques with application to point arguello oil field. AAPG (Am. Assoc. Pet. Geol.) Bull. 75. https://doi:10.1306/0c9b2939-1710-11d7-8645000102c1865d.

Niu, Z., Liu, G., Ge, J., Zhang, X., Cao, Z., Lei, Y., An, Y., Zhang, M., 2019. Geochemical characteristics and depositional environment of paleogene lacustrine source rocks in the Lufeng sag, Pearl River Mouth basin, south China sea. J. Asian Earth Sci. 171, 60–77. https://doi:10.1016/j.jseaes.2018.01.004.

Pan, S., Liu, W., 2022. Characteristics and physical property controlling factors of the low permeability reservoir of the 5th Member of Wenchang Formation for the Y Oilfield in Pearl River Mouth Basin, South China Sea[J]. Marine Geology Frontiers 38 (4), 71–79.

Pang, X., Luo, Q., Jiang, Z., Bai, G., Wang, Y., 2003. Accumulating Diversity And Its Mechanism Between Hanging And Lower Walls Of Result In Superimposed Basin. CHINESE JOURNAL OF GEOLOGY 38 (3), 413–424. https://doi:CNKI:SUN:DZKX.0.2003-03-003.

Peng, J., Pang, X., Shi, H., 2016. Hydrocarbon generation and expulsion characteristics of Eocene source rocks in the Huilu area, northern Pearl River Mouth basin, South China Sea: Implications for tight oil potential. Mar. Petrol. Geol. 72, 463–487. https://doi:10.1016/j.marpetgeo.2016.02.006.

Ruggieri, R., Trippetta, F., Cassola, T., Petracchini, L., 2022. Basin modeling constrains source rock position and dimension in the Burano-Bolognano petroleum system (Central Italy). J. Asian Earth Sci. 240, 105436.

Schowalter, T.T., 1979. Mechanics of Secondary Hydrocarbon Migration and Entrapment. AAPG (Am. Assoc. Pet. Geol.) Bull. 63. https://doi:10.1306/2f9182ca-16ce-11d7-8645000102c1865d.

Sibson, R.H., Moore, J., , M. M., Rankin, A.H., 1975. Seismic pumping—a hydrothermal fluid transport mechanism. J. Geol. Soc. 131 (6), 653–659. https://doi:10.1144/gsjgs.131.6.0653.

Dreyer, T., Scheie, A., Walderhaug, O., 1990. Mini permeameter-based Study of Permeability Trends in Channel Sand Bodies. AAPG (Am. Assoc. Pet. Geol.) Bull. 74, 359–374.

Trippetta, F., Ruggieri, R., Brandano, M., Giorgetti, C., 2020. Petrophysical properties of heavy oil-bearing carbonate rocks and their implications on petroleum system evolution: Insights from the Majella Massif. Mar. Petrol. Geol. 111, 350–362.

Wang, T., Dong, S., Wu, S., 2016. Numerical simulation of hydrocarbon migration in tight reservoir based on Artificial Immune Ant Colony Algorithm: A case of the Chang 81 reservoir of the Triassic Yanchang Formation in the Huaqing area, Ordos Basin, China. Mar. Petrol. Geol. 78, 17–29. https://doi:10.1016/j.marpetgeo.2016.09.003.

Wang, X., Zhang, X., Lin, H., 2019. Geological structure characteristics of central anticline zone in Lufeng 13 subsag Pearl River Mouth Basin and its control effect of hydrocarbon accumulation. Acta Pet. Sin. 56–66. https://doi:CNKI:SUN:SYXB.0.2019-01-004.

Wang, W., Wang, G., Hu, J., 2020. Characteristics of Fluid Inclusions and Hydrocarbon Charging Periods of Lower Yanchang Formation in Central Ordos Basin. China. 2020. J. Earth Sci. Environ. 24 (2), 159–171. https://doi: 10.19814/j.jese.2019.08024.

Wang, F., Chen, D., Wang, Q., 2021. Quantitative evaluation of sandstone carrier transport properties and their effects on hydrocarbon migration and accumulation: A case study of the Es32 in the southern slope of Dongying Depression, Bohai Bay Basin. Mar. Petrol. Geol. 126, 104937. https://doi:10.1016/j.marpetgeo.2021.104937.

Xiang, C., Xia, B., Xie, X., 2004. Major hydrocarbon migration pathway system in western slope zone of Songliao basin. Oil Gas Geol. 2004 (2), 204–208+215.

Yahi, N., Schaefer, R.G., Littke, R., 2001. Petroleum Generation and Accumulation in the Berkine Basin, Eastern Algeria. AAPG (Am. Assoc. Pet. Geol.) Bull. 85 (8), 1439–1467. https://doi:10.1306/8626CAD7-173B-11D7-8645000102C1865D.

Yang, W., Wang, R., Wu, J., Chen, Y., Gan, S., Zhong, W., 2015. An efficient and effective common reflection surface stacking approach using local similarity and plane-wave flattening. J. Appl. Geophys. 117, 67–72. https://doi:10.1016/j.jappgeo.2015.02.029.

Zhang, H., Jin, Z., 2000. Present situation and the future of petroleum migration research in our country. J. Univ. Pet., China (Ed. Nat. Sci.) 24 (4), 1–3.

Zhang, L., Luo, X., Liao, Q., 2010. Quantitative evaluation of synsedimentary fault opening and sealing properties using hydrocarbon connection probability assessment. AAPG (Am. Assoc. Pet. Geol.) Bull. 9 (94), 1379–1399. https://doi:10.1306/12140909115.

Zhang, X., Wang, X., Shu, Y., 2017. Geological characteristics and forming conditions of large and medium oilfields in Lufeng Sag of Eastern Pearl River Mouth Basin. J. Cent. S. Univ. 48 (11), 2979–2989. https://doi:10.11817/j.issn.1672-7207.2017.11.019.

Zhang, Q., Wu, X., Ahmed, E., 2022. Diagenesis of continental tight sandstone and its control on reservoir quality: A case study of the Quan 3 member of the cretaceous Quantou Formation, Fuxin uplift. Songliao Basin. Mar. Petrol. Geol. 145. https://doi:10.1016/j.marpetgeo.2022.

Zhu, X., Ge, J., Wu, C., 2019. Reservoir characteristics and main controlling factors of deep sandstone in Lufeng sag, Pearl River Mouth Basin [J]. Acta Pet. Sin. 40 (S1), 69–80.

Zhu, C., Gang, W., Zhao, X., Chen, G., Pei, L., Wang, Y., Yang, S., Pu, X., 2022. Reconstruction of oil charging history in the multi-source petroleum system of the Beidagang buried-hill structural belt in the Qikou Sag, Bohai Bay Basin, China: Based on the integrated analysis of oil-source rock correlations, fluid inclusions and geologic data. J. Petrol. Sci. Eng. 208 (B), 109197. https://doi:10.1016/j.petrol.2021.109197.

Zhuravljov, A., Lanetc, Z., Khoperskaya, N., 2021. A simple approach to increasing computational efficiency of numerical simulations of hydrocarbon migration based on the Darcy flow concept. Comput. Geosci. 157, 104915. https://doi:10.1016/j.cageo.2021.104915.